Mid Infrared Properties of Low Metallicity Blue Compact Dwarf Galaxies from *Spitzer/IRS*

Yanling Wu,[1] V. Charmandaris,[2,1,3] Lei Hao,[1] B. R. Brandl,[4] J. Bernard-Salas,[1] H. W. W. Spoon,[1] J.R. Houck[1]

wyl@astro.cornell.edu, vassilis@physics.uoc.gr, haol@isc.astro.cornell.edu, brandl@strw.leidenuniv.nl, jbs@isc.astro.cornell.edu, spoon@isc.astro.cornell.edu, jrh13@cornell.edu

ABSTRACT

We present a *Spitzer*-based mid-infrared study of a large sample of Blue Compact Dwarf galaxies (BCD) using the Infrared Spectrograph (IRS), including the first mid-IR spectrum of IZw18, the archetype for the BCD class and among the most metal poor galaxies known. We show the spectra of Polycyclic Aromatic Hydrocarbon (PAH) emission in low-metallicity environment. We find that the equivalent widths (EW) of PAHs at 6.2, 7.7, 8.6 and $11.2\,\mu$m are generally weaker in BCDs than in typical starburst galaxies and that the fine structure line ratio, [NeIII]/[NeII], has a weak anti-correlation with the PAH EW. A much stronger anti-correlation is shown between the PAH EW and the product of the [NeIII]/[NeII] ratio and the UV luminosity density divided by the metallicity. We conclude that PAH EW in metal-poor high-excitation environments is determined by a combination of PAH formation and destruction effects.

Subject headings: dust, extinction – galaxies: abundances – galaxies: starburst – galaxies: dwarf – infrared: galaxies

1. Introduction

Galaxies formed in the early Universe are likely to have very different properties from typical evolved galaxies in the local Universe because they were formed from an environment

---

[1]Astronomy Department, Cornell University, Ithaca, NY 14853, USA

[2]University of Crete, Department of Physics, P. O. Box 2208, GR-71003, Heraklion, Greece

[3]Chercheur Associé, Observatoire de Paris, F-75014, Paris, France

[4]Leiden Observatory, 2300 RA Leiden, The Netherlands

deficient in heavy elements. Important as they are, those primeval galaxies are beyond the capability of current mid-IR instruments, thus motivating an ongoing effort to identify local analogs of the galaxy formation process in the early Universe.

Blue compact dwarfs are a group of extra-galactic objects with faint, blue optical colors, small sizes and low metallicities. They are generally dominated by one or more recent bursts of star formation. Early studies hinted that BCDs have dramatically different properties compared to normal dwarf galaxies (Arp 1965; Zwicky 1966). Accumulated observational evidence over the recent years provided more details on the unique properties of these galaxies (for a review see Kunth & Östlin 2000). Early ground based observations by Roche et al. (1991) on the mid-IR spectra of 60 galaxies revealed that PAH emission is generally suppressed in low-metallicity galaxies, which could be due to hard photons destroying the particles that produce the unidentified infrared bands. Thuan et al. (1999) has shown that there is no sign of these bands in the mid-IR spectrum of SBS0335-052E taken by the Infrared Space Observatory (ISO). The suppression of the PAH emission is also seen in the mid-IR spectra of 4 BCDs discussed by Madden et al. (2000); Galliano et al. (2005); Madden et al. (2005). Dwek (2004) proposed that the delayed injection of carbon molecules into the interstellar medium(ISM) might be partly responsible for the absence of PAH features in young star forming regions, or for the existence of a metallicity threshold below which PAHs have not formed. Hogg et al. (2005) suggested that the lack of PAH emission is closely related to the low luminosity of their sample. More recent work based on *Spitzer* observations has confirmed that PAH emission is missing in the most metal-poor galaxies (Houck et al. 2004b; Engelbracht et al. 2005). Hunt et al. (2005) studied the global spectral energy distributions (SEDs) of 7 BCDs and confirmed that those SEDs deviate significantly from the standard templates of "classical", evolved and massive starburst galaxies, in the sense that the far-infrared (FIR) spectra peak at/or shortward of $60\,\mu$m and mid-IR spectra show little or no PAH emission. Having a relatively low metallicity, these galaxies are at an early epoch of their evolution, making them similar to samples of the distant, more massive protogalaxies, thus allowing us to study the star formation and chemical enrichment in an environment likely to be similar to that in the early Universe.

Recently, mid-IR imaging and spectroscopy of a handful of such systems revealed the presence of dusty embedded sources as well as fine structure line emission in their spectra, consistent with a hard radiation field from massive young stars (Thuan et al. 1997; Madden et al. 2000, 2005). In general, short bursts (1-5 Myr) of intensive star formation are found to best match the data (Mas-Hesse & Kunth 1999). Some BCDs appear to be very rapid star formers, and thus true dwarf analogs of giant starbursts (Kunth & Östlin 2000). The profiles and strengths of the PAHs, which might be good tracers of star formation, vary substantially (Förster Schreiber et al. 2004).

Using the unprecedented sensitivity of the Infrared Spectrograph (Houck et al. 2004a) on the *Spitzer* Space Telescope (Werner et al. 2004), we compiled a large sample of of the lowest metallicity galaxies known. Since little information on their mid-IR fluxes were available from literature, a large fraction of them were first observed with the peak-up cameras at 16 and 22 μm. As we discuss in detail in the following section, those which were bright enough were observed spectroscopically. In this paper we present 5.2–36 μm spectra of 12 galaxies for which the signal-to-noise ratio (SNR) was high enough to perform a quantitative analysis on the strength of the spectral features, as well as 16 and 22 μm broad band imaging for the remaining of the sample, covering metallicities from 1/50 Z$_\odot$ to 0.65 Z$_\odot$. Many of the remainders are scheduled for re-observation to achieve higher SNR. In Section 2, we describe the sample, the observing strategy, and the data reduction. Section 3 presents the spectral features observed in each source while our analysis on these properties is shown in Section 4. We summarize our conclusions in Section 5. Throughout this work, we assume a ΛCDM cosmology with H$_0$ = 71 km s^{-1} Mpc^{-1}, Ω_m = 0.3 and Ω_λ = 0.7.

2. Observations and Data Reduction

A total of 61 BCDs have been observed as part of the *IRS* Guaranteed Time Observation (GTO) program. The sample included targets from the Second Byurakan Survey (SBS), Bootes Void galaxies (Kirshner et al. 1981; Popescu & Hopp 2000), and several well-known BCDs. Some basic properties of these galaxies and the observing parameters, such as: source names, right ascension (RA), declination (Dec), redshift, *Spitzer* aorkeys, observation date, and on-source integration time for each module and peak-up mode are listed in Table 1.

We used all four *IRS* modules, Short-Low (SL, 5.2-14.5 μm), Long-low (LL, 14.0-38.0 μm), Short-High (SH, 9.9-19.6 μm) and Long-high (LH, 18.7-37.2 μm) to obtain spectra for 26 sources which were expected to be sufficiently bright for spectroscopy. SBS1200+589B was the only one of the targets that was not observed in SL. The low resolution modules (SL, LL) produce spectra with a resolution of 64–128 while the high-resolution modules (SH, LH) have a resolution of $\sim$600 (see Houck et al. 2004a). Nearly all targets were acquired using red peak-up (RPU) mode. In the process, an image of the source at 22μm was obtained in Double Correlated Sampling (DCS) mode and it was used to locate the mid-IR centroid of the source which was then offset to the appropriate slit (see Spitzer Observers Manual for more details). For BCDs that were too faint for spectroscopy, we only obtained broad band imaging at 16 μm (13.5-18.7 μm) and 22 μm (18.5-26.0 μm) using both *IRS* peak-up cameras in Raw Data Collection (RAW) mode. Details on this method of imaging with *IRS*, also called CHEAP for Cornell High-Efficiency Advanced Peak-up, and its photometric

advantages compared to the usual *IRS* Peakup Only mode are discussed in Charmandaris et al. (2004). Eight of our galaxies were so faint in the mid-IR that only an upper limit of $\sim$0.1mJy could be established for their 16 and 22μm flux densities.

The data were processed by the *Spitzer* Science Center (SSC) data reduction pipeline version 11.0 and 11.4[1]. The 2-D image data were converted to slopes after linearization correction, subtraction of darks, and cosmic ray removal. The DCS peak-up imaging data were processed on the ground to remove cosmic rays and the residual noise of the electronics. Fixed aperture photometry was then performed in order to obtain the counts of the science target. The conversion to flux density was based on a number of calibration stars for which peak-up images, *IRS* spectra, and reliable templates are available (Cohen et al. 2003). The reduction of the spectral data started from the intermediate pipeline products (droop files), which only lacked stray light and flat field correction. Individual pointings to each nod position of the slit were co-added using median averaging and for SL and LL spectra, the two apertures were differenced in order to remove the contribution of the background. The 2-D images were extracted with the Spectral Modeling, Analysis, and Reduction Tool (SMART Ver. 5.5.1 Higdon et al. 2004) using a variable width aperture, which scales the extraction aperture with wavelength to recover the same fraction of the diffraction limited instrumental point-spread-function (PSF). The data from SH and LH were extracted using the full slit extraction method from the median of the combined images. Since no sky (off–position) measurements were taken, the contribution of the sky emission was not subtracted from SH and LH spectra. Then the spectra were flux calibrated by multiplication with the Relative Spectral Response Function (RSRF), which was created from the *IRS* standard stars α Lac for SL and LL and ξ Dra for SH and LH for which accurate templates were available (Cohen et al. 2003). We built our RSRFs by extracting the spectra of the calibration stars in the exact same way as the science targets, and dividing the stellar templates by the extracted stellar spectra. We produced one RSRF for each nod position in order to avoid systematic flat field errors. The signal difference between the nod positions provide the error estimates. Finally, the flux calibrated spectra of each order and module of the low-resolution modules except 1st order LL (LL1) (20–36μm) were scaled, using LL1 spectrum to define the continuum (presented in Fig.1 and 2). The associated photometric points are also presented on the spectra in Fig.1 and 2.

---

[1]The usage of data products from two versions of the pipeline was a result of the extended time-span over which sample was observed and the delivery of the files from the SSC. The difference between the two versions is very small and it does not introduce any inhomogeneity in the sample or influence the conclusions of the paper.

3. Results

From the 26 BCDs observed spectroscopically, only 11 produced spectra with SNR sufficient for features to be measured (SNR ≥ 2 in the 5–8μm range of the 2nd order SL, SL2). These spectra are presented in Fig.1 and 2. We also include the first mid-IR spectrum of IZw18[2]. The 22 μm flux density of each target with an aperture radius of 7.2″ measured during its acquisition using the red peak-up camera (circle), as well as a "synthetic" 22 μm flux obtained by convolving the spectrum with the filter response function (square) are indicated in the Fig.1 and 2. The $IRAC$ 8 μm (asterisk) and $MIPS$ 24 μm (triangle) flux densities are also indicated when available (Engelbracht et al. 2005). One can see that for all point sources, including SBS0335-052E, NGC1140, Mrk1499, Mrk1450, CG0598, CG0752, UM461 and IZw18, the two broad band values for the RPU agree very well. NGC1140 is marginally saturated at 22 μm, but we correct for this effect based on the PSF profile. The agreement of the spectra and the photometric measurements indicates the internal consistency of the calibration of the instrument between spectroscopy and peak-up photometry when all spectra are scaled to LL1. However, as expected, for sources which are extended or well above the 340 mJy saturation limit of red peak-up in a 8.4 second exposure time, such as NGC1569, IIZw40, Haro11 and UGC4274, there is a disagreement among these photometric measurements (See Fig.1 and 2).

It is clearly seen from Fig. 1 and 2 that the forbidden transitions of [SIV] at 10.51 μm and [NeIII] at 15.55 μm are visible even in the low-resolution spectra, while [NeII] at 12.81 μm, [SIII] at 18.71 μm and [SiII] at 34.8 μm lines are seen in most of them. The line fluxes used in the analysis are determined from high-resolution spectra (See Fig.3). The emission from PAHs at 6.2, 7.7, 8.6 11.2 and 12.8 μm are also clear in several of our targets and they are indicated in the figures but no pronounced silicate emission or absorption features are present. All PAH measurements presented in this paper were measured from the low-resolution spectra.

3.1. Mid infrared Morphology

As mentioned in Section 2, all spectroscopic observations were preceded by an acquisition using the 22μm peak-up camera. This provided not only more precise position of the objects for telescope pointing, but also deep 22 μm images of our targets. Analysis of those images

---

[2]The overall shape of the mid-IR continuum is evident from Fig. 1, but a measurement of spectral features is challenging due to the noise in the spectrum.

indicates that with the exception of four galaxies: NGC1569, UGC4274, IIZw40 and Haro11, all other targets are unresolved at $22\,\mu$m (FWHM=6.5″) . In Fig.4, we display the $22\,\mu$m images of these four galaxies, overlayed with the spectrograph slits as they were placed when the spectra were obtained. Among those targets NGC1569 shows the most complex structure with two bright cores in the mid-IR. This source also has very extended emission in the optical. Therefore, not surprisingly, it requires a large scaling factor of $\leq 80\%$ when we "stitch" the spectra of 1st order SL (SL1) and 2nd order LL (LL2), mostly due to the different slit widths and orientations between the two low-resolution modules. In UGC4274, we find that most of its $22\,\mu$m flux originates from a compact unresolved knot while a similar peak is seen in the near infrared which is offset by $\sim 3''$ from the mid-IR one.

3.2.   Individual Objects

IZw18 — This is the first identified member of the blue compact dwarf galaxy class (Searle & Sargent 1972) and until recently[3] held the record of a galaxy with the lowest metallicity at Z $\sim$0.02 Z$_\odot$ (Skillman & Kennicutt 1993). IZw18 is located at a distance of 12-15 Mpc and is a bona fide young galaxy and no red giant branch stars are seen(Izotov et al. 2004). Zwicky (1966) described it as a double system of compact galaxies, which are in fact two star-forming regions, a northwest component and a southeast one, separated by an angular distance of 5.8″. Examination of the spatial distribution of the stellar populations suggest that the star formation process is still building the main body from inside out (Izotov et al. 2004). Both Izotov et al. (1997a) and Legrand et al. (1997) detected several broad emission components in this BCD, suggesting that Wolf-Rayet (WR) features can also exist in extremely low metallicity environment. It is intrinsically very faint in the infrared. The first mid-IR spectrum of IZw18 is presented in Fig.1. As we discuss in the subsequent sections we are able to estimate the mid-IR spectral slope from its low-resolution spectrum. The fine structure lines of [SIV] and [NeIII] can clearly be seen in its high-resolution spectrum, though the identification of [NeII] and [SIII] is not yet firm. A much deeper observation with more exposure time has been scheduled and the new spectrum will be presented in a future paper (Wu et al. in prep 2006).

---

[3]Only this year (2005) measurements of Izotov et al. (2005) showed that the brightest star formation region of the western component of SBS0335-052 has an oxygen abundance of only 12+log(O/H)=7.12±0.03 ($\sim$0.017 Z$_\odot$), suggesting it is the most metal poor galaxy known.

SBS0335-052E — Currently the third most metal-poor galaxy known with 0.024 $Z_\odot$ (Izotov et al. 1997b), SBS0335-052E is at a distance of 58 Mpc. Thuan et al. (1997) found that stars in SBS0335-052E are younger than ∼100 Myr and the current burst of star formation is no older than 5 Myrs, thus making it a truly young system. This galaxy is unexpectedly bright in the mid-IR (Thuan et al. 1999; Houck et al. 2004b) with roughly 75% of the total luminosity coming from the mid-IR (Plante & Sauvage 2002). It has six compact regions of massive star formation, five of which are visible and one obscured, and all of them lying within a diameter of 526 pc (Thuan et al. 1997). There is no sign of PAH emission in its spectrum and silicate absorption at $9.7\,\mu$m is clearly seen. The SED of the galaxy is dominated by a very strong continuum, which unlike typical star forming galaxies, such as NGC7714 (Brandl et al. 2004), peaks at ∼28 μm (f_ν), indicating the presence of little cold dust. The fine structure lines of [NeIII] and [SIV] are present, though not very strong.

UM461 — This is a dwarf galaxy with a double nucleus and is found at a distance of 15 Mpc. It has an external envelope which is strongly distorted towards the South-West, suggesting a recent tidal event (Doublier et al. 1999). The metallicity of UM461 is ∼0.087 $Z_\odot$ (Kniazev et al. 2004). With only 168 seconds of integration time in SL module, the obtained spectrum is very noisy. However, the fine structure lines, such as [SIV], [NeIII] and [SIII] can be clearly seen longward of $10\,\mu$m. The identification of PAH emission is doubtful and an upper limit of $0.199\,\mu$m for the PAH EW at $11.2\,\mu$m is indicated in Table 4.

Haro11 — This is a metal poor galaxy with ∼0.1 $Z_\odot$ (Bergvall et al. 2000). Its distance is ∼88 Mpc and it has an infrared luminosity, L_{IR} of 1.8×10^{11} $L_\odot$[4]. Haro11 is a moderately strong radio source, with spatially extended continuum emission at 6 and 20 cm(Vader et al. 1993; Heisler & Vader 1995). Multiple nuclei are apparent on optical broad band images (Heisler & Vader 1994) as well as narrow-band Hα images (Heisler & Vader 1995). All three nuclei are similar in continuum stellar emission (Heisler & Vader 1995) and spectra of the nuclei confirm that they are all at the same distance (Vader et al. 1993). The PAH features are much weaker compared with NGC1140 but the fine structure lines of [SIV], [SIII], [NeIII] and [NeII] lines are clearly present.

Mrk1450 — A dwarf compact object with a projected dimension less than 1 kpc, Mrk1450 is located at a distance of ∼14 Mpc. Its optical images display moderately de-

---

[4]Calculated from the *IRAS* flux densities following the prescription of Sanders & Mirabel (1996): $L_{IR}=5.6\times10^5 D_{Mpc}^2(13.48S_{12} + 5.16S_{25} + 2.58S_{60} + S_{100})$.

formed circular isophotes and a central star forming component. A strong color gradient is present reaching a $B - R$ ~2.2 mags at the outskirts of the galaxy, while the surface brightness distribution obeys an $r^{1/4}$ law (Doublier et al. 1997). This galaxy has an L_{IR}[5] less than 1.8×10^8 $L_\odot$. Its metallicity is ~0.12 $Z_\odot$ (Izotov & Thuan 1999). Due to the low SNR in SL2, PAH emission can not be identified clearly below 10μm, even though the 11.2 μm and possibly 12.8 μm PAHs are present. The fine structure lines of [SIV] and [NeIII] are strong.

IIZw40 — This is a prototypical H II galaxy (Sargent & Searle 1970) with L_{IR}[6] less than 2.9×10^9 $L_\odot$ at a distance of ~10 Mpc. The metallicity of this galaxy is ~0.17 $Z_\odot$ (Cerviño & Mas-Hesse 1994). It consists of a compact, extremely bright core and two fan-like structures, which have been interpreted as the result of a merger between two small galaxies (Baldwin et al. 1982; Brinks & Klein 1988). Star formation is concentrated in the nucleus while the double structure is quite red and shows no star formation activity (Cairós et al. 2001). Hα emission is very strong, contributing 40% to the R−band flux at the nucleus. The starburst could be very young and its strength is rather extraordinary (Deeg et al. 1997). It also displays WR features (Conti 1991). Our mid-IR spectrum indicates that the PAHs are present, though extremely weak. The fine structure lines of [SIV], [SIII], [NeII] and [NeIII], have been detected.

NGC1569 — A nearby dwarf galaxy (D~2.2 Mpc Israel 1988) which has a metallicity of ~0.19 $Z_\odot$ (Kobulnicky & Skillman 1997) and is currently in the aftermath of a massive burst of star formation (Waller 1991), with L_{IR} of 5.8×10^8 $L_\odot$. It lies close to the plane of the Galaxy and therefore its optical properties are strongly affected by the Galactic dust extinction (Kinney et al. 1993). The presence of a broad emission feature around 4650 Å and a broad base to the Hα line indicate that WR stars are present in the nucleus of NGC1569 (Ho et al. 1995). It contains two bright super star clusters. The very hot, bright nucleus of this galaxy resembles a superluminous, young star cluster (Arp & Sandage 1985). The fine structure lines of [SIV] and [NeIII] are stronger compared to [SIII] and [NeII], which can be seen clearly even in the low-resolution spectrum (See Fig.2). The PAH features are clearly present. As discussed by Galliano et al. (2003, 2005), the mid-IR emission is dominated by small grains.

---

[5]For this galaxy, the *IRAS* 12 μm and 25 μm flux densities are calculated by convolving our spectrum with the *IRAS* filters. The 100 μm flux density is an upper limit, thus making the L_{IR} also an upper limit.

[6]For this galaxy, only upper limit exists for *IRAS* 100 μm, thus making the L_{IR} also an upper limit.

Mrk1499 — This is an irregular galaxy displaying a very blue elongated central structure with two components in the optical, the brightest being off-centered with respect to the outer contours (Doublier et al. 1997). These authors suggested that this structure is reminiscent of "double nuclei" objects, while Petrosian et al. (2002) argued that this could be just an observational artifact. It has an L_{IR}[7] of 1.3×10^9 $L_\odot$ and is at a distance of $\sim$38 Mpc. An oxygen abundance of $\sim$ 0.3 $Z_\odot$ has been derived from the line measurements of Petrosian et al. (2002), using the N2 calibrator (Denicoló et al. 2002), which allows us to calculate the oxygen abundance based on the [NII]/Hα ratio. PAH features are prominent and several fine structure lines are detected. In this particular galaxy, the SNR in SL2 is rather poor, thus making the definition of the continuum challenging. We measured the $6.2\,\mu$m PAH EW by defining a maximum and minimum local continuum and then averaging the two measurements.

NGC1140 —This is a blue irregular galaxy at a distance of $\sim$25 Mpc, containing large mass of ionized gas in its center (Kinney et al. 1993). Its metallicity is $\sim$0.4 $Z_\odot$ (Calzetti 1997). Lamb et al. (1986) concluded that NGC1140 has experienced a single burst of star formation and its population mainly consists of main-sequence stars with a contribution from supergiants and, possibly, WR stars. Hunter et al. (1994) used the Hubble Space Telescope (*HST*) Planetary Camera to study the central supergiant H II region and found that the central 1/2 kpc of NGC1140 contains $\sim$7 blue, luminous, compact super star clusters. It has a very small average size of grains (Galliano et al. 2003, 2005) and a L_{IR} of 4.3×10^9 $L_\odot$. The low resolution mid-IR spectrum shows pronounced PAH emission, almost comparable to that in the typical starburst galaxy NGC7714, while the fine structure lines are stronger compared with NGC7714.

UGC4274 — A galaxy also known as NGC2537 and Mrk86, UGC4274 is extended in the mid-IR (see Fig.3) and is located at a distance of $\sim$7 Mpc. It has a large, very irregular nucleus consisting of $\sim$80 star-forming knots distributed in a circular region which is surrounded by a red envelope (Gil De Paz 2000). The Hα image shows a very complex gas distribution, with multiple filaments, loops and twisted features (Cairós et al. 2001). It has an L_{IR} of 5.0×10^8 $L_\odot$ and emission from PAHs dominates its spectrum. An oxygen abundance of 12+log(O/H)=8.05 (Z$\sim$0.13 $Z_\odot$) has been derived by Meier et al. (2001) based on the relationship between B magnitude and metallicity. Since this method has a large uncertainty and there is no direct spectroscopically measured oxygen abundance available,

---

[7]For this galaxy, only *IRAS* $60\,\mu$m and $100\,\mu$m are available. For *IRAS* $12\,\mu$m and $25\,\mu$m, we convolved our spectrum with the two *IRAS* filters and calculated their values.

we calculated the metallicity using the N2 calibrator. A value of 12+log(O/H)=8.52±0.13 (Z∼0.41 $Z_\odot$) has been derived from the line measurement in Ho et al. (1997). All major mid-IR fine structure lines of the galaxy are very strong.

CG0598 — This is a galaxy selected from the Bootes Void sample. It is at a distance of 253 Mpc and it has an L_{IR}[8] less than 5.9×10^{10} $L_\odot$. In the optical, this galaxy is a flattened disk system with a bright, round nucleus. It has a smooth, elongated surrounding disk which is asymmetric with respect to the nucleus (Cruzen et al. 1997). The metallicity of this galaxy is ∼ 0.65 $Z_\odot$ (Peimbert & Torres-Peimbert 1992). In Fig.2, we can see that CG0598 shows very strong PAH emission in all bands and the usual fine structure lines of [NeII], [NeIII], [SIV] and [SIII] can be identified.

CG0752 — This galaxy is ∼91 Mpc away with an L_{IR}[9] of 2.2×10^{10} $L_\odot$. It has remained uncatalogued for a long time because of its proximity to bright star (Sanduleak & Pesch 1987). PAH emission is moderately strong and the fine structure lines of [SIV], [SIII], [NeIII] and [NeII] are present. There is no measured oxygen abundance available from literature for this galaxy.

4.   Analysis

4.1.   The mid-infrared spectral slope of BCDs

The photometric properties and metallicities of the 53 galaxies in our BCD sample (excluding the 8 objects that were too faint in mid-IR) are listed in Table 2. The 16 and $22\,\mu$m flux densities of the sources are based on broad band imaging using the blue or red peak-up cameras, while the B and K magnitudes are taken from literature. For the 12 BCDs with good IRS spectra, we also calculated their "synthetic" 16 and $22\,\mu$m flux densities by convolving the spectra with the *IRS* peak-up filters. For comparison, we list those values in Table 3. We also present the 22 to $16\,\mu$m flux density ratio, f_{22}/f_{16} ($f_{22} \equiv f_\nu(22\,\mu m)$)in Table 2. This ratio provides the mid-IR slope of the spectrum and can be a useful probe of the shape of the mid-IR SED even if the galaxy are too faint to obtain a spectrum. One of

---

[8]The *IRAS* $12\,\mu$m and $25\,\mu$m flux densities are calculated by convolving the spectrum with the *IRAS* filters. The *IRAS* $100\,\mu$m flux density is an upper limit thus making L_{IR} an upper limit as well.

[9]The *IRAS* $12\,\mu$m flux density is calculated by convolving the spectrum with the *IRAS* filter.

our sources, SBS0335-052E, has a particularly low value of f_{22}/f_{16}, indicating the absence of cold dust around the central star forming region. As discussed by Houck et al. (2004b), the SED of SBS0335-052E peaks maximum f_ν at a much shorter wavelength of $\sim 28\,\mu$m while most normal galaxies peak longward of $60\,\mu$m.

We explore the variation on the f_{22}/f_{16} ratio as a function of metallicity in Fig.5a. In addition to the 12 BCDs, we include in this figure a typical starburst galaxy NGC7714 (Brandl et al. 2004), and an Ultra-Luminous Infrared Galaxy (ULIRG), UGC5101 (Armus et al. 2004), in order to sample a wider range of different types of galaxies forming massive young stars. The BCDs with only photometric CHEAP images are included using crosses as well when their metallicities are available from literature. It has been pointed out by Hunter et al. (1989) that no clear metallicity dependence is observed in mid-IR and FIR colors of normal galaxies. This is also confirmed in Fig.5a where the f_{22}/f_{16} ratio for all the BCDs seems to have an average value of $\sim$2.5 and shows no metallicity dependence.

In Fig.5b and 5c, we plot the ratio of the flux density at $22\,\mu$m to the $IRAC$ $8\,\mu$m band, f_{22}/f_8, as well as the $MIPS$ $24\,\mu$m to the $IRAC$ $8\,\mu$m, f_{24}/f_8, as a function of their metallicities. The $IRAC$ $8\,\mu$m and $MIPS$ $24\,\mu$m flux densities are calculated by convolving the mid-IR spectra of these BCDs with the appropriate filter profiles. Engelbracht et al. (2005) observed that the $8\,\mu$m to $24\,\mu$m color changes markedly between 1/3 to 1/5 solar metallicity and suggested that this change is predominantly due to a decrease in the $8\,\mu$m emission. Our Fig.5b and 5c are very similar to Fig.2 in their paper. It appears that there is a separation on the f_{24}/f_8 ratio around 1/5 $Z_\odot$ on our plots with the exception of SBS0335-052, which as mentioned earlier shows no PAH detection.

It is very important to note that, as shown by our data, using the f_{22}/f_8, or f_{24}/f_8 ratios to infer the strength of the PAH emission is not a very robust method. Since the $7.7\,\mu$m and $8.6\,\mu$m PAH emission is included in the $IRAC$ $8\,\mu$m band, one might expect that a lower f_{22}/f_8 ratio would indicate the presence of a stronger PAH emission from the galaxy. However, a low f_{22}/f_8 ratio can also be due to decreased emission at $22\,\mu$m, resulting from the lack of cooler dust. A galaxy with a flat continuum but no PAH emission can have the same f_{22}/f_8 ratio as a galaxy which shows strong PAH emission and a steep continuum. If we consider SBS0335-052E and UGC4274, we can see that they have a very similar f_{22}/f_8 ratio, even though no PAHs are detected in SBS0335-052E while PAHs are prominent in UGC4274. This can be understood when we take into account the f_{22}/f_{16} ratio. It is evident from Fig.5a that these two sources have very different mid-IR spectral slopes. This explains why SBS0335-052E lies away from the upper left corner of Fig.5a. We have also plotted the PAH EW at $6.2\,\mu$m and $11.2\,\mu$m as a function of the f_{24}/f_8 ratio in Fig.6a and 6b. We can see that overall a lower f_{24}/f_8 value indicates a stronger PAH emission, but

there are some measurements that deviate from this trend. For completeness we also present the PAH EW at $6.2\,\mu$m and $11.2\,\mu$m as a function of f_{22}/f_{16} in Fig.6c and 6d but no clear correlation can be seen.

4.2.   PAH and metallicity

In Section 1, we mentioned that the absence of PAH emission could be due to the low abundance of carbon and/or nucleating grains. In SBS0335-052E, the most metal poor galaxy for which a high quality mid-IR spectrum is available, there is an upper limit of just $0.018\,\mu$m in the EW of the 6.2μm feature (Houck et al. 2004b). To examine a possible variation in the PAH EW with metallicity, we plotted the PAH EW of $6.2\,\mu$m and $11.2\,\mu$m for our sample as function of their metallicity in Fig.7. The PAH EW were derived by integrating the flux of the feature in the mean spectra of both nod positions above an adopted continuum, and then divided by the average continuum flux in the integration range. The baseline was determined by fitting a spline function to the selected points. The wavelength limits for the integration of the features were approximately $5.95\,\mu$m to $6.55\,\mu$m for the $6.2\,\mu$m PAH, $7.15\,\mu$m to $8.20\,\mu$m for the $7.7\,\mu$m PAH, $8.20\,\mu$m to $8.90\,\mu$m for the $8.6\,\mu$m PAH and $10.80\,\mu$m to $11.80\,\mu$m for the $11.2\,\mu$m PAH feature. Here we only plot the $6.2\,\mu$m and $11.2\,\mu$m PAH EW, but measurements on the $7.7\,\mu$m and $8.6\,\mu$m PAH EW can be found in Table 4. We can see that PAH emission is absent in the most metal-poor BCDs and its strength is generally suppressed in a low metallicity environment. This result is contrary to what has been found in typical starburst galaxies where the PAH EW is much stronger with values greater than $0.5\,\mu$m for the $6.2\,\mu$m and $7.7\,\mu$m PAH bands (i.e. Brandl et al. 2004; Brandl et al. in prep 2005). In Fig.7, it appears that there is a trend showing that galaxies with a lower metallicity may have smaller PAH EW. Except for the two galaxies which have large uncertainty in their oxygen abundance, the PAH EW and metallicity seem to correlate quite well. The errors in the EW indicated in Fig.7 vary from one source to the other and are mainly due to the different SNR among the sources. Quantifying this relation by a least-squares (logarithmic) fit gives us a slope of N=1.57±0.63 for the $6.2\,\mu$m PAH EW and N=1.16±0.36 for the $11.2\,\mu$m PAH EW. This weak trend we are seeing that the PAH EW is probably related to metallicity effects agrees with the relation suggested by Hogg et al. (2005) and Engelbracht et al. (2005).

4.3.   The hardness of the radiation field

The presence of a young starburst in a low metallicity environment results in the production of high energy photons which can propagate relatively large distances before being

absorbed by the metals in the ISM. High-resolution *IRS* spectra were taken of 26 galaxies and the results for the 12 BCDs that we discussed above are summarized in Fig.3 and Table 4. Because of the rather large difference in the ionization potentials of Ne^{++} (41eV) and Ne^+ (22eV), the ratio of [NeIII]/[NeII] is a good tracer of the hardness of the interstellar radiation field (Thornley et al. 2000). The [SIV]/[SIII] ratio, another indicator of the hardness of the radiation field has also been studied in this paper. Given the fact that extinction in mid-IR is only a few percent of the optical extinction (Draine 2003), those line ratios are far less sensitive to the differential extinction compared to optical or UV lines. We plot the two line ratios in Fig.8. Since the extinction effects on [NeIII] ($15.55\,\mu$m) and [NeII] ($12.81\,\mu$m) are similar, the ratio of [NeIII]/[NeII] is only weakly affected by extinction, while for [SIV]/[SIII], we indicate the effect of differential extinction by the arrow on the upper left corner of the plot for an A_v of $\sim$13 mag.

We also studied the dependence of [NeIII]/[NeII] ratio on metallicity and the results are presented in Fig.9. We find that our 11 BCDs (CG0752, which has no metallicity measurements in literature, is not included.) appear to define a band, where galaxies with lower metallicity display a higher [NeIII]/[NeII] ratio, thus harboring a harder radiation field. For a given [NeIII]/[NeII] ratio, there is significant scatter within metallicities. This scatter could be due to local variations or differential/patchy dust extinction in these systems. It also suggests that the metallicity may not be the only factor that affects the hardness of the radiation field. The results on the [SIV]/[SIII] ratio are plotted in Fig.10 and we can see that it shares a similar trend as the [NeIII]/[NeII] ratio. For the discussion that follows we choose the [NeIII]/[NeII] ratio since it is less dependent on the extinction and the neon lines are generally stronger. Further more, the [NeIII] and [NeII] lines span a wider range in ionization potential than [SIV] and [SIII].

4.4. PAH and the [NeIII]/[NeII] ratio

As discussed by Madden et al. (2000), PAHs are at best a minor dust component in dwarf galaxies. In Fig.11, we plot the EW of the 6.2 and $11.2\,\mu$m PAHs as a function of the hardness of the radiation field, using [NeIII]/[NeII] as an indicator. We observe that the PAH EWs at 6.2 and $11.2\,\mu$m are generally suppressed in a harder radiation field as indicated by a larger [NeIII]/[NeII] ratios, suggesting that the deficiency in PAH emission may be related to the destruction of the photodissociation region (PDR) by hard UV photons. However, the trend we see is weak. A conventional least-squares fit that minimizes (logarithmic) residuals in PAH EW yields a slope of N=-0.91$\pm$0.31 for the 6.2 μm PAH and N=-0.92$\pm$0.27 for the $11.2\,\mu$m PAH. In addition, we found that for a given [NeIII]/[NeII] ratio, we can

have different PAH EW values. For example Haro11 has a considerably weaker PAH EW at both $6.2\,\mu$m and $11.2\,\mu$m as compared with NGC1140 even though they have a very similar [NeIII]/[NeII] ratio. This scatter indicates that some other or additional process is in play.

4.5. PAH and luminosity density

Another important parameter of the radiation field is its UV luminosity density. Does this also play a role in the destruction of PAH molecules? In young starbursts, L_{FIR} is representative of the total UV luminosity. We estimate the luminosity density of the 12 BCDs in our sample, using the $22\,\mu$m luminosity. Takeuchi et al. (2005) show that there is linear relation between the mid-IR luminosities ($12\,\mu$m or $25\,\mu$m) and the total infrared luminosity, even though Dale et al. (2005) has shown a peak-to-peak uncertainty of a factor of 5 in using the $24\,\mu$m luminosity to indicate the total infrared luminosity for their sample of starburst galaxies. We calculate $L_{22\mu m}$ using the 22μm images obtained with the red peak-up camera and divide it by the estimated volume (V) of the objects from their optical or infrared images[10]. This should be proportional to the UV luminosity density. The results are listed in Table 5. We present the 6.2 and 11.2μm PAH EW as a function of the 22μm luminosity density in Fig.12. There are fewer data points on the plot compared to the table since we do not have PAH EW measurement for all the galaxies in Table 5. We can see that there is a trend that PAH EW decreases with increasing luminosity density. However, this relation is somewhat weak. A least-squares fit (logarithmic) of the slope returns N=-0.63±0.21 for the $6.2\,\mu$m PAH and N=-0.77±0.18 for the $11.2\,\mu$m PAH. There is considerable scatter on this plot. For instance, SBS0335-052E and Haro11 have very similar $L_{22\mu m}$/V value, but we have not found any PAH emission in SBS0335-052E while PAHs are weak but clearly present in Haro11.

A plot of the dependence of the PAH EW as a function of the product of the hardness of the radiation field and the luminosity density, [NeIII]/[NeII]*$L_{22\mu m}$/V is presented in Fig. 13. We observed that it is better correlated than both the PAH EW vs [NeIII]/[NeII] and PAH EW vs luminosity density. A least-squares fit (logarithmic) returns N=-0.39±0.12 for $6.2\,\mu$m PAH and N=-0.47±0.10 for $11.2\,\mu$m PAH. This suggests that an increased density of harder photons destroys more PAH molecules. The fact that we are seeing a better correlation on Fig.13 than in Fig.11 or Fig.12 suggests that both the luminosity density and the hardness of the radiation field contribute to the destruction of PAHs.

---

[10]We use the mid-infrared images to estimate the volume for sources that are resolved at $22\,\mu$m and the optical images for the rest of the sample.

4.6.   PAHs: formation and destruction effects

We have shown in the previous section that there are generally weaker PAHs in metal-poor environments. We have also discussed the effects of the hardness of the radiation field and the luminosity density on the destruction of PAH molecules. Is the absence of PAHs in metal-poor galaxies solely due to formation effects or destruction effects or some combination? To examine this we plot the PAH EW as a function a new quantity: $([NeIII]/[NeII]) \times (L_{22\,\mu m}/V) \times (1/Z)$, where the product of the neon ratio and the luminosity density represents the destruction effect and Z, the metallicity of the galaxy, represents the formation effect. We can see in Fig. 14 that there is a much tighter anti-correlation on this plot as compared to the previous series of plots on the PAH EW we have shown. A least-squares fit (logarithmic) gives a slope of N=-0.39±0.09 for the $6.2\,\mu m$ PAH and N=-0.43±0.08 for the $11.2\,\mu m$ PAH. We conclude that both the formation effects (Z) and the destruction effects $([NeIII]/[NeII]) \times (L_{22\,\mu m}/V)$ contribute to the weak PAH EW.

5.   Conclusions

We have explored the mid-IR properties of blue compact dwarf galaxies with *Spitzer IRS*. We obtained broad band images at 16 and $22\,\mu m$ from the *IRS* peak-up camera. Using the low-resolution *IRS* spectra, we detected emission from PAHs, at 6.2, 7.7, 8.6, 11.2 and $12.8\,\mu m$, for most of our galaxies though the strength varies considerably. We also detected a number of fine structure lines in our mid-IR spectra, including [SIV], [NeII], [NeIII] and [SIII] and found that for metallicities ranging between 1/50 $Z_\odot$ to 0.65 $Z_\odot$, the line ratios, [NeIII]/[NeII] and [SIV]/[SIII], which measure the hardness of the ionization field, vary inversely with metallicity. Our study yielded the following conclusions:

1) The ratio of f_{22}/f_{16} is ∼2.5±0.6 on average, but it does not show any dependence on metallicity.

2) Both the emission of PAHs and a hot dust component affect the f_{22}/f_8 (or f_{24}/f_8) ratio in a similar way. These effects are difficult to disentangle without mid-IR spectra or measurements of the mid-IR fluxes at several wavelengths. Predictions of the strength of PAHs based on a single pair of mid-IR broad band fluxes may be problematic and should be used with caution (see Fig. 5 and 6).

3) The emission of PAHs in metal-poor BCDs is generally suppressed (see Fig 7).

4) The product of the hardness of the radiation field as traced by the neon line ratio with the mid-IR luminosity density, a "stand in" for the intensity of UV luminosity, correlates

well with the PAH EW (see Fig. 13).

5) The product of the hardness of the radiation field and the luminosity density divided by the metallicity of the galaxies has a strong correlation with the PAH EW. This suggests that the absence of PAHs in metal-poor environment is due to a combination of formation effects and destruction effects (Fig.14).

REFERENCES

Armus, L., et al. 2004, ApJS, 154, 178

Arp, H., & Sandage, A. 1985, AJ, 90, 1163

Arp, H., & Oconnell, R. W. 1975, ApJ, 197, 291

Arp, H. 1965, ApJ, 142, 383

Baldwin, J. A., Spinrad, H., & Terlevich, R. 1982, MNRAS, 198, 535

Brandl, B. R., et al. 2004, ApJS, 154, 188

Brandl, B. R., et al. 2005, in preparation

Bergvall, N., Masegosa, J., Östlin, G., & Cernicharo, J. 2000, A&A, 359, 41

Brinks, E., Klein, U. 1988, MNRAS, 231, 63p

Charmandaris, V., et al. 2004, ApJS, 154, 142

Cairós, L. M., Caon, N., Vílchez, J. M., González-Pérez, J. N., & Muñoz-Tuñón, C. 2001, ApJS, 136, 393

Calzetti, D. 1997, AJ, 113, 162

Cerviño, M., & Mas-Hesse, J. M. 1994, A&A, 284, 749

Cohen, M., Megeath, T.G., Hammersley, P.L., Martin-Luis, F., & Stauffer, J. 2003, AJ, 125, 2645

Conti, P. S. 1991, ApJ, 377, 115

Cruzen, S. T., Weistrop, D., & Hoopes, C. G. 1997, AJ, 113, 1983

Dale, D. A. et al. 2005, astro-ph/0507645

De Vaucoulers, G., De Vaucoulers, A., Corwin Jr., H. G., Buta, R. J. Paturel, G., & Fouque, P. 1991, Third Reference Catalogue of Bright Galaxies, version 3.9

Deeg, H.-J., Duric, N., & Brinks, E. 1997, A&A, 323, 323

Denicoló, G., Terlevich, R., & Terlevich, E. 2002, MNRAS, 330, 69

Dwek, E. 2004, in "The Spectral Energy Distribution of Gas-Rich Galaxies: Confronting Models with Data", Heidelberg, 4-8 Oct. 2004, eds. C.C. Popescu and R.J. Tuffs, AIP Conf. Ser., in press, astro-ph/0412344

Doublier, V., Comte, G., Petrosian, A., Surace, C., & Turatto, M. 1997, A&AS, 124, 405

Doublier, V., Caulet, A., & Comte, G. 1999, A&AS, 138, 213

Draine, B. T. 2003, ARA&A, 41, 241

Engelbracht, C. W., Gordon, K. D., Rieke, G. H., Werner, M. W., Dale, D. A., & Latter, W. B. 2005, ApJ, 628, L29

Förster Schreiber, N. M., Roussel, H., Sauvage, M., & Charmandaris, V. 2004, A&A, 419, 501

Gallego, J., Zamorano, J., Rego, M., & Vitores, A. G. 1997, ApJ, 475, 502

Galliano, F. Madden, A. P., Jones, C. D., Wilson, J.-P., & F. Le Peintre 2003, A&A, 407, 159

Galliano, F., Madden, S. C., Jones, A. P., Wilson, C. D., & Bernard, J.-P. 2005, A&A, 434, 867

Gil de Paz, A. 2000, Ph.D thesis

Gil de Paz, A., Madore, B. F., & Pevunova, O. 2003, ApJS, 147, 29

Guseva, N. G., Papaderos, P., Izotov, Y. I., Green, R. F., Fricke, K. J., Thuan, T. X., & Noeske, K. G. 2003, A&A, 407, 91

Guseva, N. G., Papaderos, P., Izotov, Y. I., Green, R. F., Fricke, K. J., Thuan, T. X., & Noeske, K. G. 2003, A&A, 407, 105

Heisler, C. A., & Vader, J. P. 1994, AJ, 107, 35

Heisler, C. A., & Vader, J. P. 1995, AJ, 110, 87

Higdon, S. J. U., et al. 2004, PASP, 116, 975

Ho, L. C., Filippenko, A. V., & Sargent, W. L. W. 1997, ApJS, 112, 315

Ho, L. C., Filippenko, A. V., & Sargent, W. L. 1995, ApJS, 98, 477

Hogg, D. W., Tremonti, C. A., Blanton, M. R., Finkbeiner, D. P., Padmanabhan, & N., Quintero, A. D., Schlegel, D. J., & Wherry, N. 2005, ApJ, 624, 162

Houck, J. R, et al. 2004, ApJS, 154, 18

Houck, J. R., et al. 2004, ApJ, 154, 211

Hunt, L., Bianchi, S., & Maiolino, R. 2005, A&A, 434, 849

Hunter, D. A., Gallagher, J. S., Rice, W. L., & Gillett, F. C. 1989, ApJ, 336, 152

Hunter, D. A., O'Connell, R. W., & Gallagher, J. S. 1994, AJ, 108, 84

Israel, F. P. 1988, A&A, 198, 109

Izotov, Y. I., Foltz, C. B., Green, R. F., Guseva, N. G., & Thuan, T. X. 1997, ApJ, 487, L37

Izotov, Y. I., Lipovetsky, V. A., Chaffee, F. H., Foltz, C. B., Guseva, N. G., & Kniazev, A. Y. 1997, ApJ, 476, 698

Izotov, Y. I., & Thuan, T. X. 1999, ApJ, 511, 639

Izotov, Y. I., & Thuan, T. X. 2004, ApJ, 616, 768

Izotov, I. I., Thuan, T. X, & Gauseva, N. G. 2005, Aj accepted

Jarrett, T. H., Chester, T., Cutri, R., Schneider, S. E., & Huchra, J. P. 2003, AJ, 125, 525

Kinman, T. D., & Davidson, K. 1981, ApJ, 243, 127

Kinney, A. L., Bohlin, R. C., Calzetti, D., Panagia, N., & Wyse, R. F. G. 1993, ApJS, 86, 5

Kirshner, R. P., Oemler, A., Schechter, P. L. & Shectman, S. A., 1981, ApJ, 248, l57

Kniazev, A. Y., Pustilnik, S. A., Grebel, E. K., Lee, H., & Pramskij, A. G. 2004, ApJS, 153, 429

Kniazev, A. Y., et al. 2000, A&A, 357, 101

Kniazev, A. Y., Arkhyz, N., Engels, D., Pustilnik, S. A., Ugryumov, A. V., & Masegosa, J. 1998, IAU Circ., 6900, 1

Kobulnicky, H. A., & Skillman, E. D. 1997, ApJ, 489, 636

Kunth, D. & Östlin, G. 2000, A&A Rev., 10, 1

Lamb, S. A., Hjellming, M. S., Gallagher, J. S., & Hunter, D. A. 1986, Star Formation in Galaxies, ed. J. C. Lonsdale persson(NASA CP-2466), 259

Lauberts, A., & Valentijn, E. A. 1989, Garching: European Southern Observatory, —c1989

Legrand, F., Kunth, D., Roy, J.-R., Mas-Hesse, J. M., & Walsh, J. R. 1997, A&A, 326, L17

Madden, S. C. 2000, New Astronomy Review, 44, 249

Madden, S. C. Galliano, F., Jones, A. P., Sauvage, M. 2000, A&A, (accepted astro-ph/0510086)

Mas-Hesse, J. M., & Kunth, D. 1999, A&A, 349, 765

Masegosa, J., Moles, M. & Campos-Aguilar, A. 1994, apj, 420, 576

Meier, D. S., Turner, J. L., Crosthwaite, L. P., & Beck, S. C. 2001, AJ, 121, 740

Papaderos, P., Izotov, Y. I., Fricke, K. J., Thuan, T. X., & Guseva, N. G. 1998, A&A, 338, 43

Peimbert, M., & Torres-Peimbert, S. 1992, A&A, 253, 349

Petrosian, A. R., Movsessian, T., Comte, G., Kunth, D., & Dodonov, S. 2002, A&A, 391, 487

Plante, S. & Sauvage, M. 2002, AJ, 173,25

Popescu, C. C., & Hopp, U. 2000, A&AS, 142, 247

Roche, P. F., Aitken, D. K., Smith, C. H., & Ward, M. J. 1991, MNRAS, 248, 606

Sanders, D. B, & Mirabel, I. F. 1996, ARA&A, 34,749

Sanduleak, N., & Pesch, P. 1987, ApJS, 63, 809

Sargent, W. L. W., & Searle, L. 1970, ApJ, 162, L155

Schaerer, D., Contini, T., & Pindao, M. 1999, A&AS, 136, 35

Searle, L. & Sargent, W. L. W. 1972, ApJ, 173, 25

Skillman, E. D. & Kennicutt, R. C. 1993, ApJ, 411,655

Spinoglio, L., Malkan, M. A., Rush, B., Carrasco, L., & Recillas-Cruz, E. 1995, ApJ, 453, 616

Stasinska, G., & Leitherer, C. 1996, ApJS, 107, 661

Takeuchi, T. T., Buat, V., Iglesias-Páramo, J., Boselli, A., & Burgarella, D. 2005, A&A, 432, 423

Thornley, M. D., Schreiber, N. M. F., Lutz, D., Genzel, R., Spoon, H. W. W., Kunze, D., & Sternberg, A. 2000, ApJ, 539, 641

Thuan, T. X., Sauvage, M., & Madden, S. 1999, ApJ, 516, 783

Thuan, T. X., Izotov, Y. I., & Lipovetsky, V. A. 1997, ApJ, 477, 661

Thuan, T. X. 1983, ApJ, 268, 667

Tully, R. B., Boesgaard, A. M., Dyck, H. M., & Schempp, W. V. 1981, ApJ, 246, 38

Vader,J. P., Frogel, J. .A. Terndrup, D. A., & Heisler, C. A. 1993, AJ, 106, 1743

Vennik, J., Hopp, U., & Popescu, C. C. 2000, A&AS, 142, 399

Vitores, A. G., Zamorano, J., Rego, M., Alonso, O., & Gallego, J. 1996, A&AS, 118, 7

Waller, W. H. 1991, ApJ, 370, 144

Werner, M., et al. 2004, ApJS, 154,1

Wu, Yanling, et al. 2006, ApJ, in preparation

Young, C. K., & Currie, M. J. 1998, A&AS, 127, 367

Zwicky, F. 1966, ApJ, 143, 192
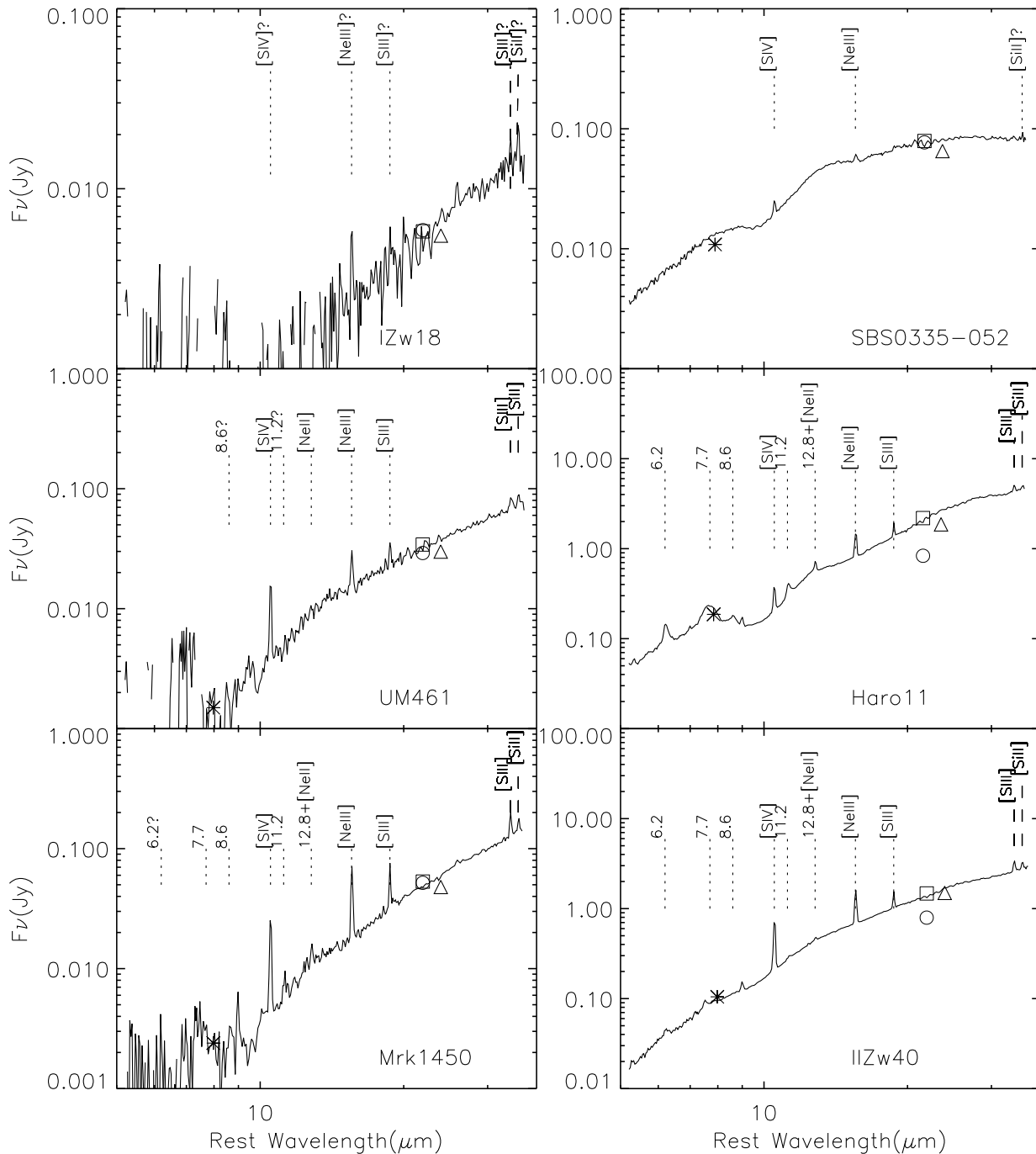
Fig. 1.— *Spitzer*/IRS mid-IR spectra of six BCDs: IZw18, SBS0335-052E, UM461, Haro11, Mrk1450 and IIZw40. The spectra of different orders were stitched and scaled to match the flux density in the 1st order LL. The circles represent the photometric flux from 22μm red peak-up camera, which has an uncertainty of 6%. The squares indicate the flux density at 22 μm measured from the spectra using "synthetic" method (See the text for detail). The asterisk and the triangle indicate the *IRAC* 8 μm and *MIPS* 24 μm measurements respectively.
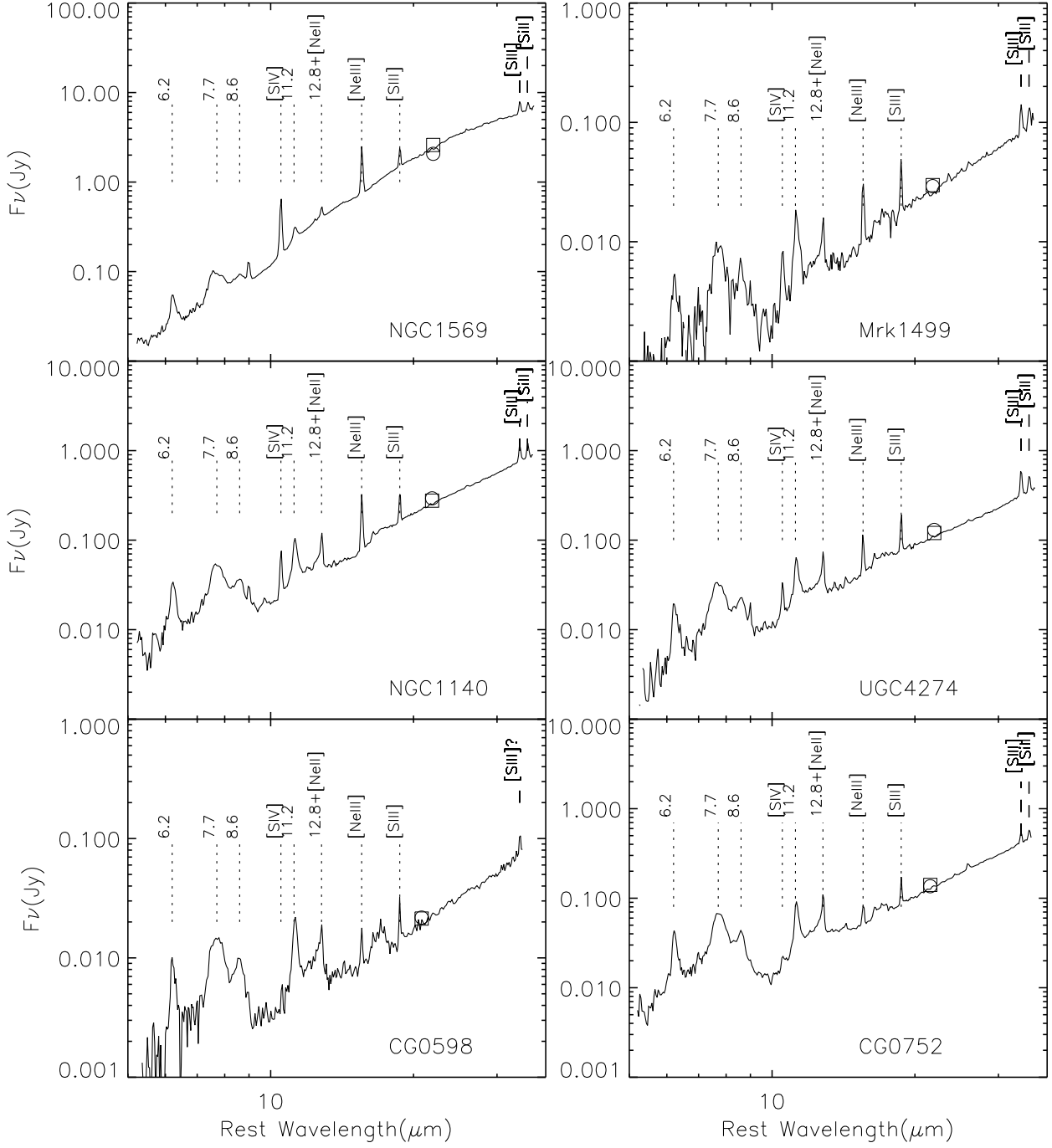
Fig. 2.— Same as Fig.1 but for another six BCDs: NGC1569, Mrk1499, NGC1140, UGC4274, CG0598 and CG0752.
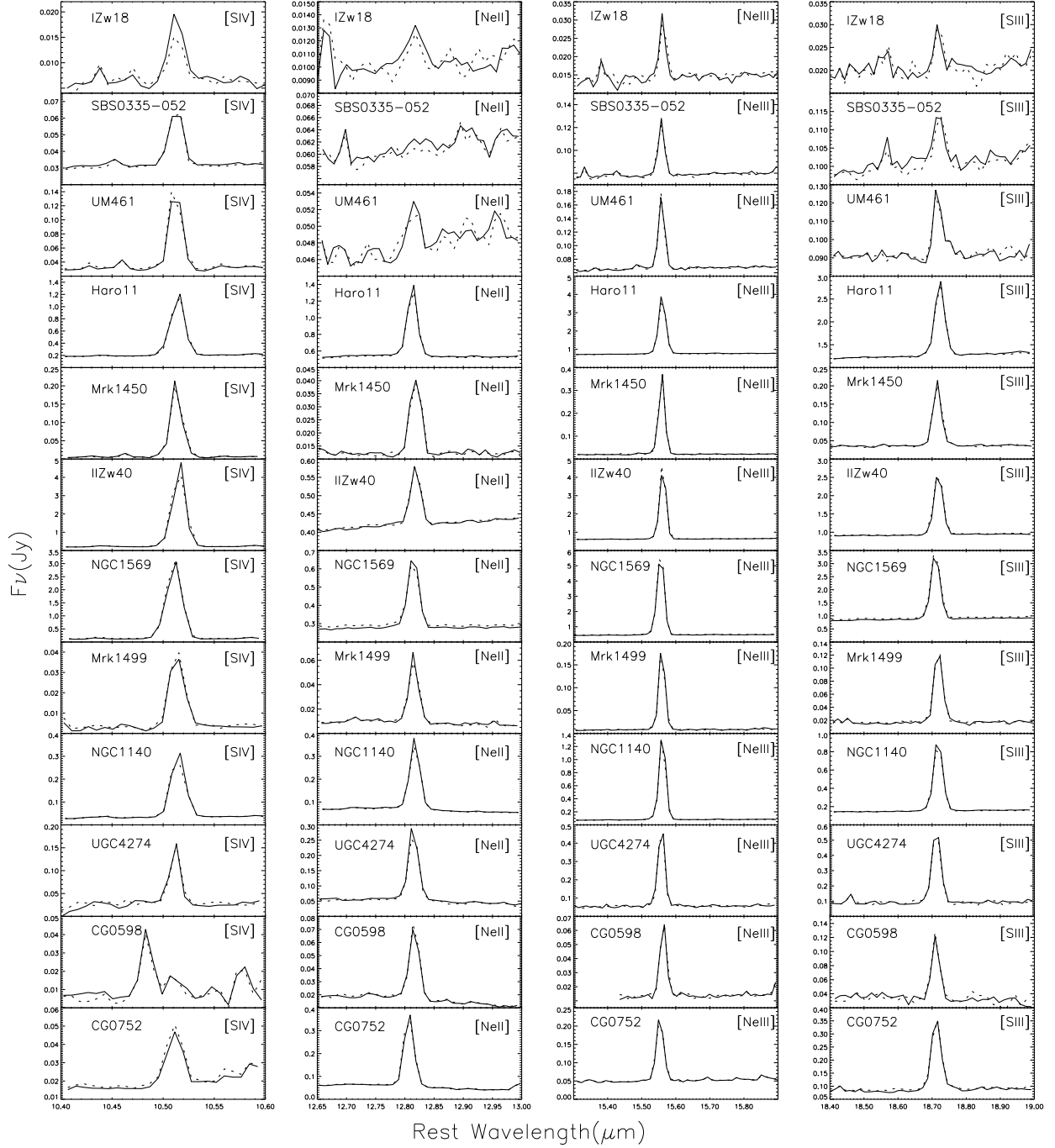
Fig. 3.— The mid-IR fine structure lines of [SIV] (10.51 μm), [NeII] (12.81 μm), [NeIII] (15.55 μm) and [SIII] (18.71 μm) from the high resolution spectra of the twelve BCDs. The solid and dotted lines denote the spectra from the first and second nod positions of the slits. Note that sky emission has not been subtracted and no stitching and scaling between different modules have been done.
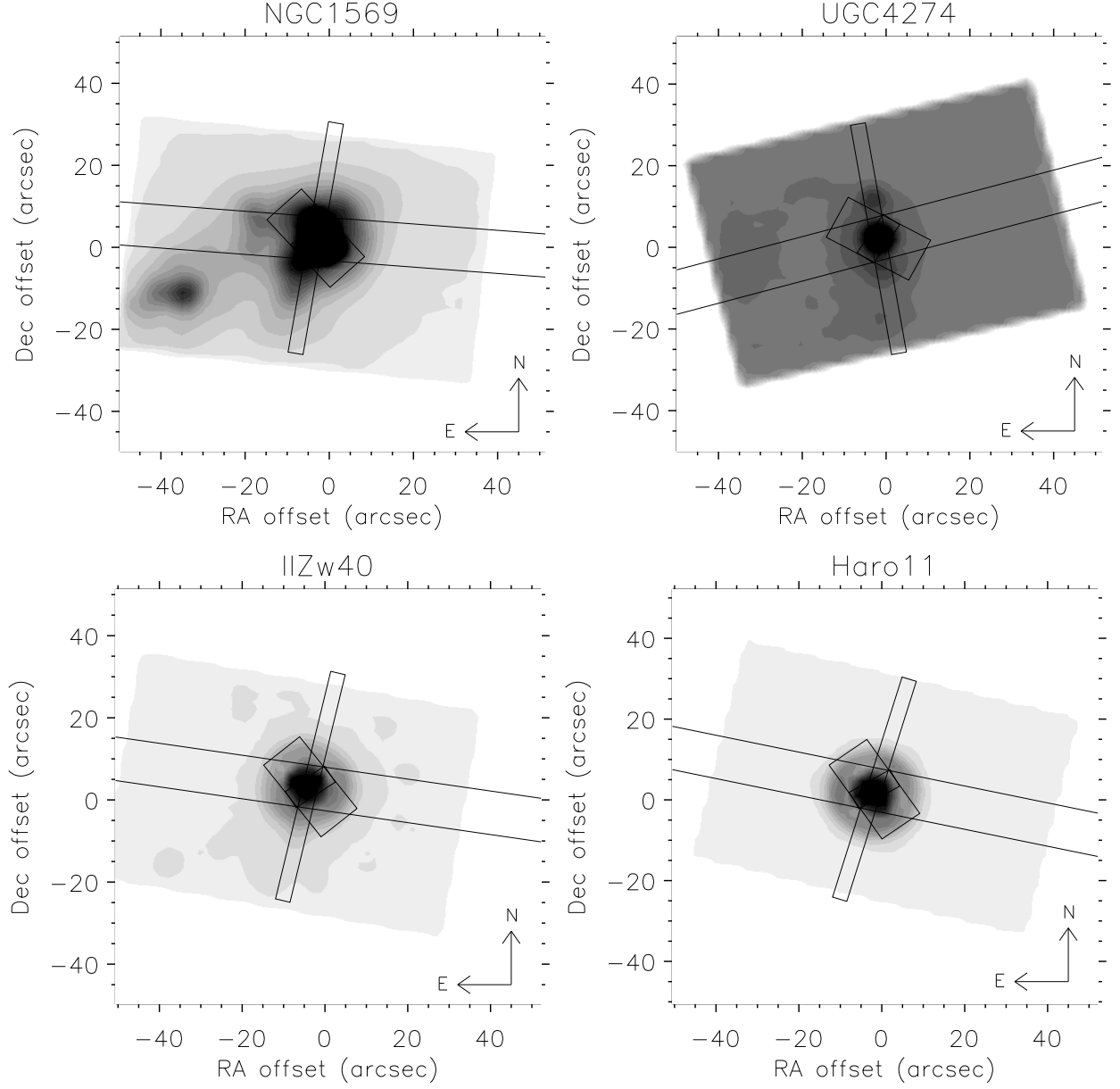
Fig. 4.— The 22 μm peak-up images of the four sources from our sample, NGC1569, UGC4274, IIZw40 and Haro11, which display extended emission. The images are overlayed with the *IRS* slits at the location from where the spectrum was obtained. The widths of the slits increase in the order of: SL, SH, LL, LH and their length in the order of: SH, LH, SL, LL.
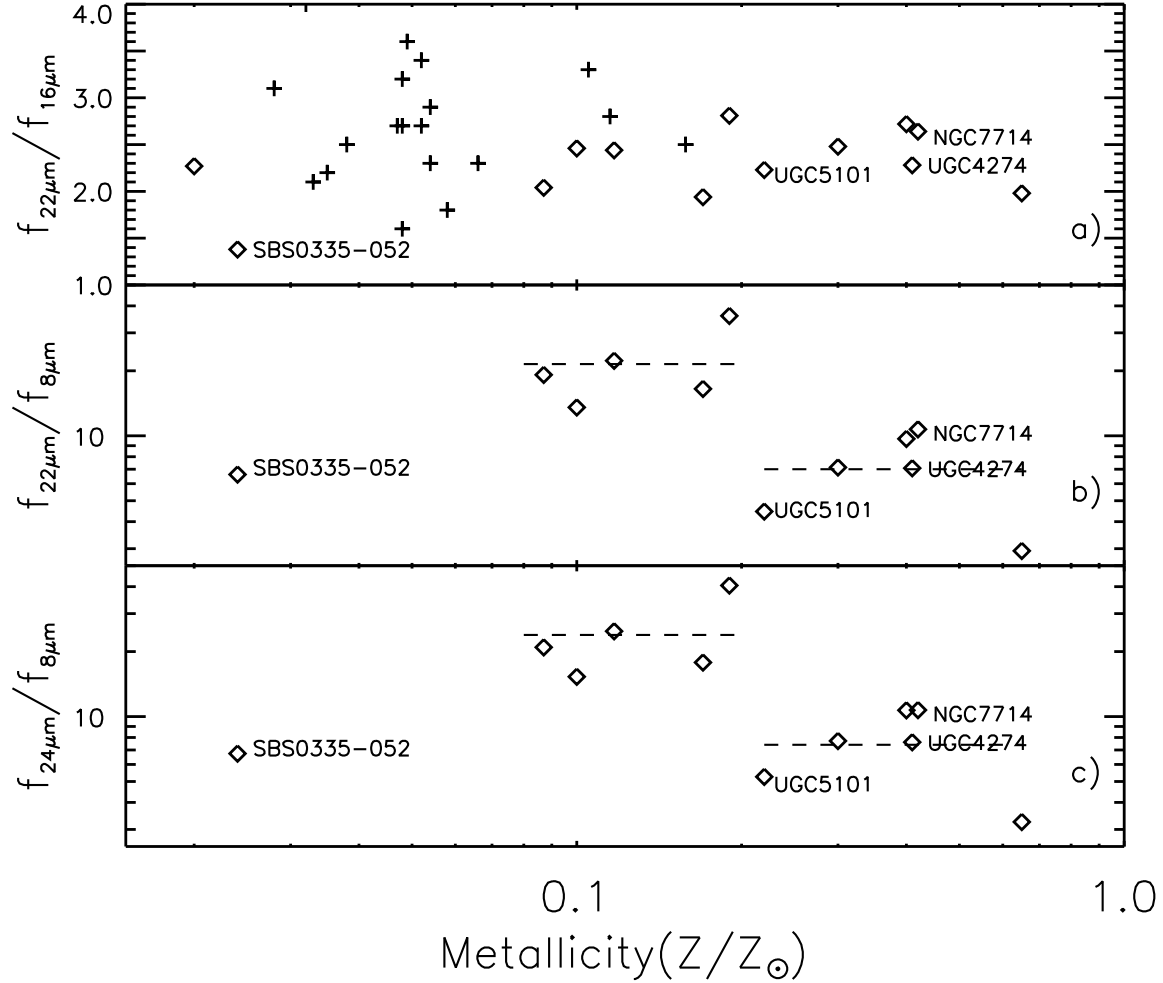
Fig. 5.— a) This figure shows the ratio of the 22 to the 16 μm flux density as a function of the metallicity of the sources. For sources with an IRS spectrum available, the ratio was calculated by convolving the spectrum with the 22 and 16μm filter curves. A starburst galaxy, NGC7714, and a ULIRG, UGC5101, are also included for comparison. Diamonds denote sources for which we have obtained spectra. The crosses indicate galaxies for which the photometric points were obtained using IRS broad band imaging (see Section 2). b) The same as a) but for the 22 to 8 μm flux density as a function of metallicity. Here we include only the galaxies for which we have full *IRS* spectra since we measure the 8 μm flux density from the spectra. SBS0335-052 clearly departs from the general trend. We indicate the average flux ratios by the dashed lines.c) Same as b) but for 24 over 8 μm flux density as a function of metallicity.
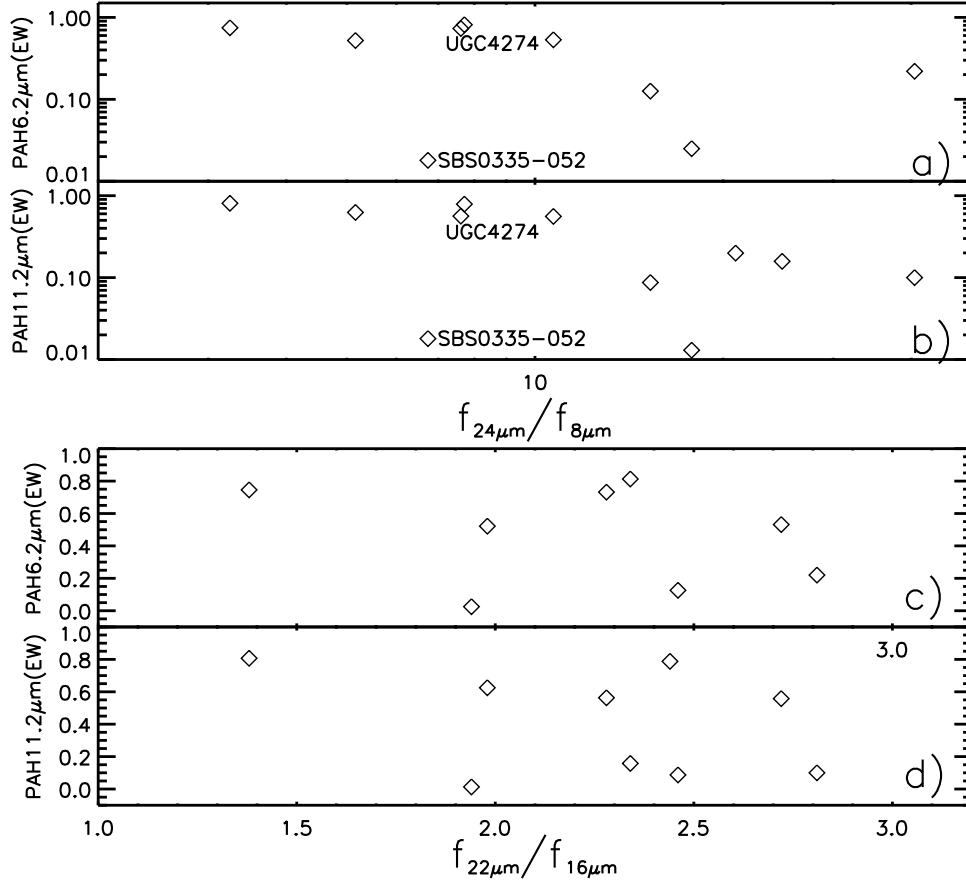
Fig. 6.— a) This figure presents the ratio of the $6.2\,\mu$m PAH EW of our galaxies as a function of the 24 over $8\,\mu$m flux ratio. We note that with some scatter generally a lower f_{24}/f_8 indicates a larger PAH EW. b) Same as a) but for the $11.2\,\mu$m PAH EW. c) Same as a) but for using the 22 over $16\,\mu$m flux density ratio as the variable. There is no clear relation between the mid-IR spectral slope as indicated by f_{22}/f_{16} and the PAH strength. d) Same as c) but for $11.2\,\mu$m PAH EW.
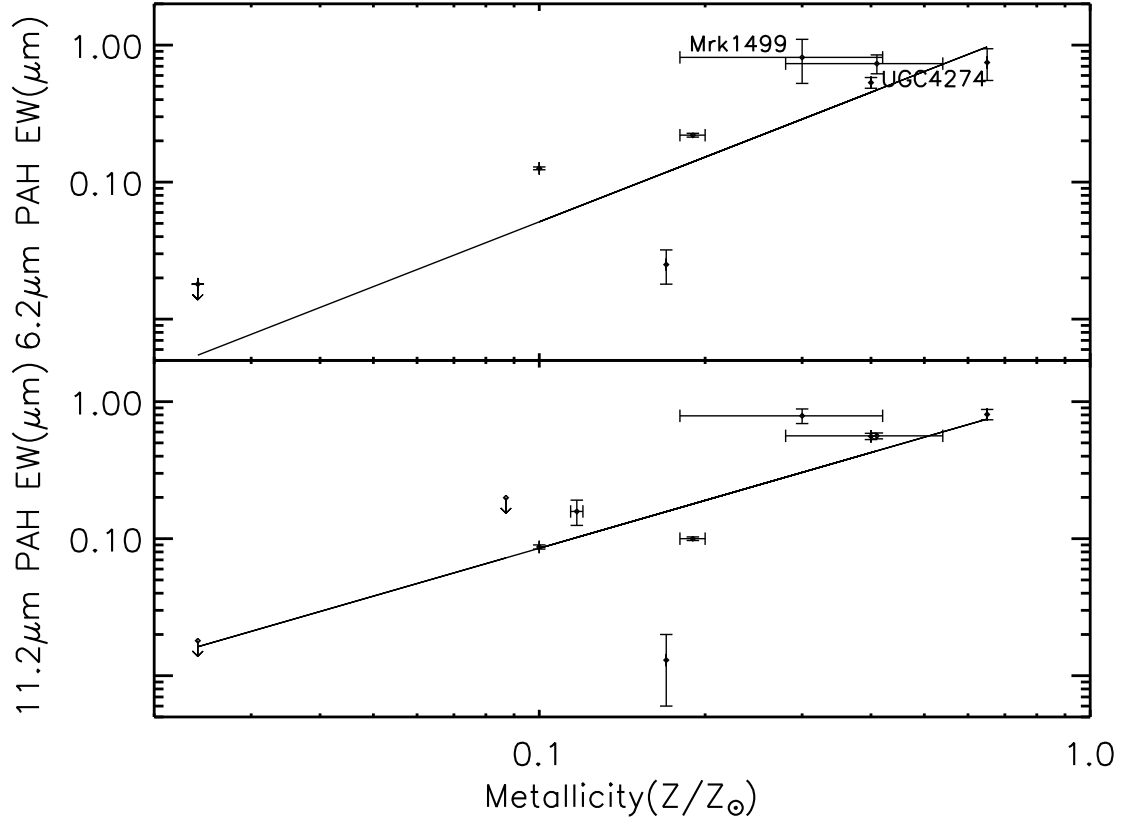
Fig. 7.— a) This figure shows the PAH EW at $6.2\,\mu$m vs metallicity. Note that the downward arrow indicates the upper limit for the PAH emission in SBS0335-052E. In some cases the extracted spectra of a target from the two nod positions of the slit differ. These uncertainties are translated into the error bars for the EW which, as we can see in Mrk1499, can be fairly large (also see text). b) Same as in a) but for the $11.2\,\mu$m PAH feature.
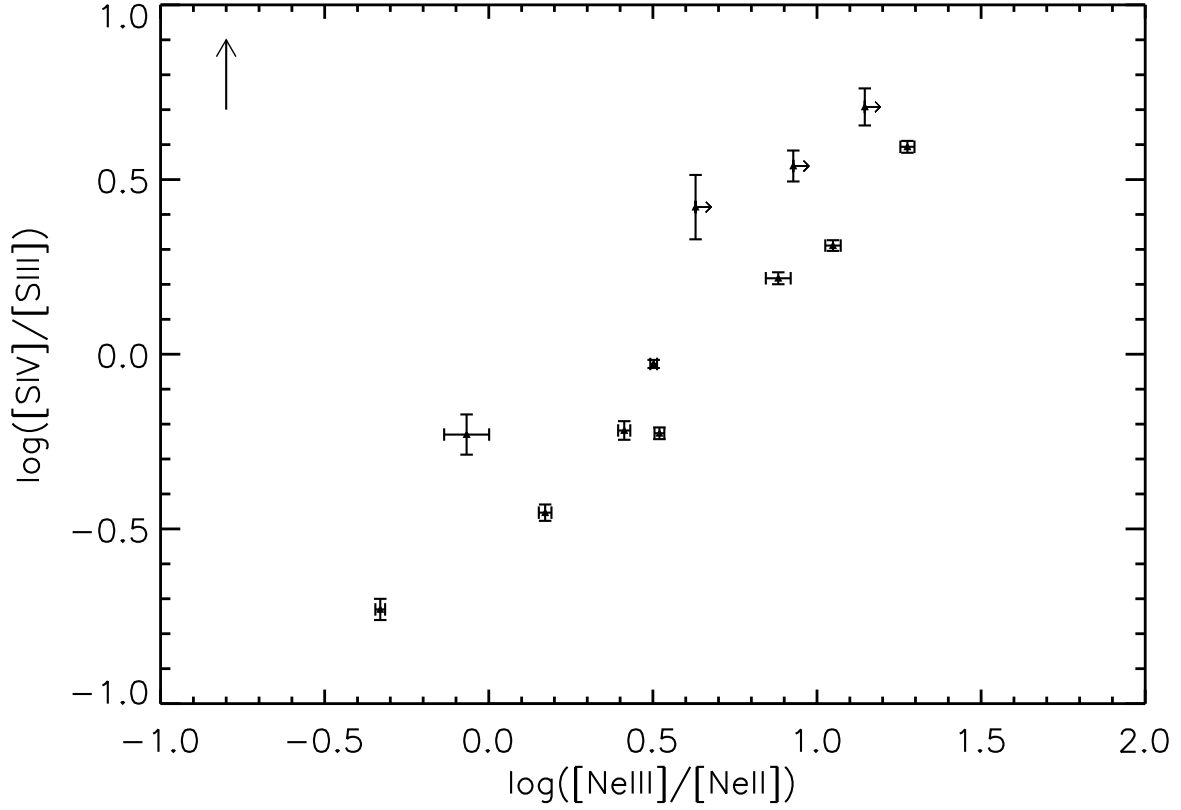
Fig. 8.— This plot shows the log([SIVλ10.51 μm]/[SIIIλ18.71 μm]) ratio as a function of log([NeIIIλ15.55 μm]/[NeIIλ12.81 μm]) for our sample. Both ratios are indicators of the hardness of the ionization field. Since no [NeII] has been detected in the high resolution spectrum of SBS0335-052, IZw18 and UM461, the lower limits of the [NeIII]/[NeIII] ratios are represented by arrows. No correction has been made for extinction. The effect of the differential extinction on the ratio of [SIV]/[SIII] is indicated by the arrow on the upper left corner for $A_v \sim 13$ mag.
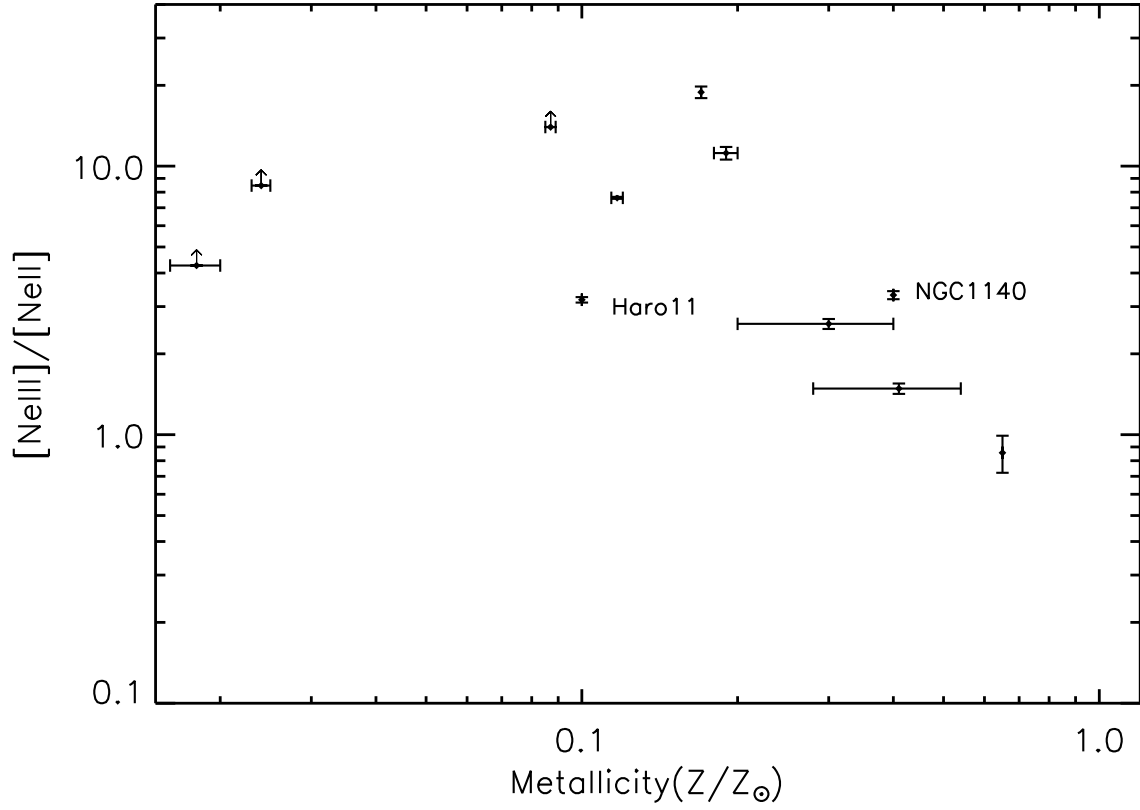
Fig. 9.— The strength of the [NeIIIλ15.55 μm]/[NeIIλ12.81 μm] ratio as a function of metallicity for our sample. The fluxes of [NeIII] and [NeII] were measured using the high resolution spectra of the sources and the metallicity (and its uncertainty) were obtained from the literature (see Table 2). Note that no [NeII] has been detected in SBS0335-052E, IZw18 and UM461, so we are showing the lower limit of [NeIII]/[NeII] by an up-pointing arrow.
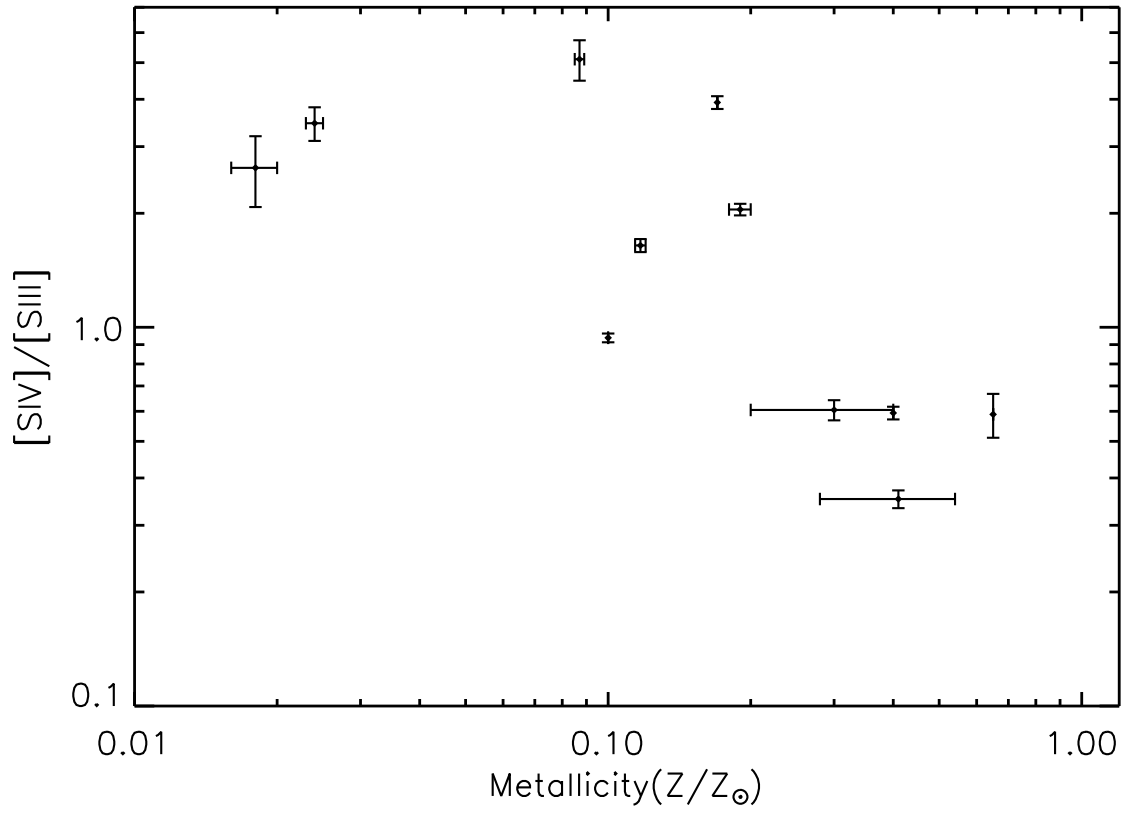
Fig. 10.— Same as Figure 8 but for [SIVλ10.51 μm]/[SIIIλ18.71 μm].
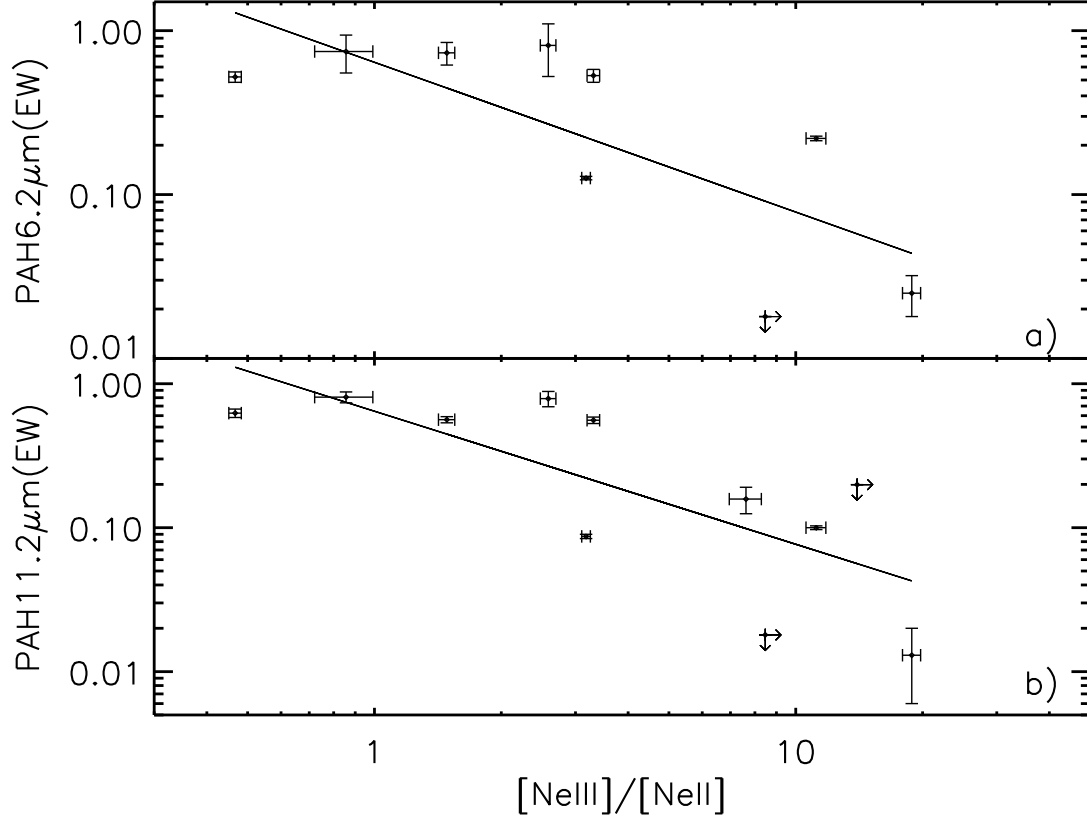
Fig. 11.— a) The EW of the $6.2\,\mu$m PAH as a function of the [NeIII]/[NeII] ratio. Note that since no PAH emission was detected in SBS0335-052E, the upper limit of its EW is indicated by a downward arrow. Similarly, the lower limit of the [NeIII]/[NeII] ratio for this source is indicated by right-pointing arrow since no [NeII] can be seen in the spectrum. b) Same as a) but for the 11.2 μm PAH.
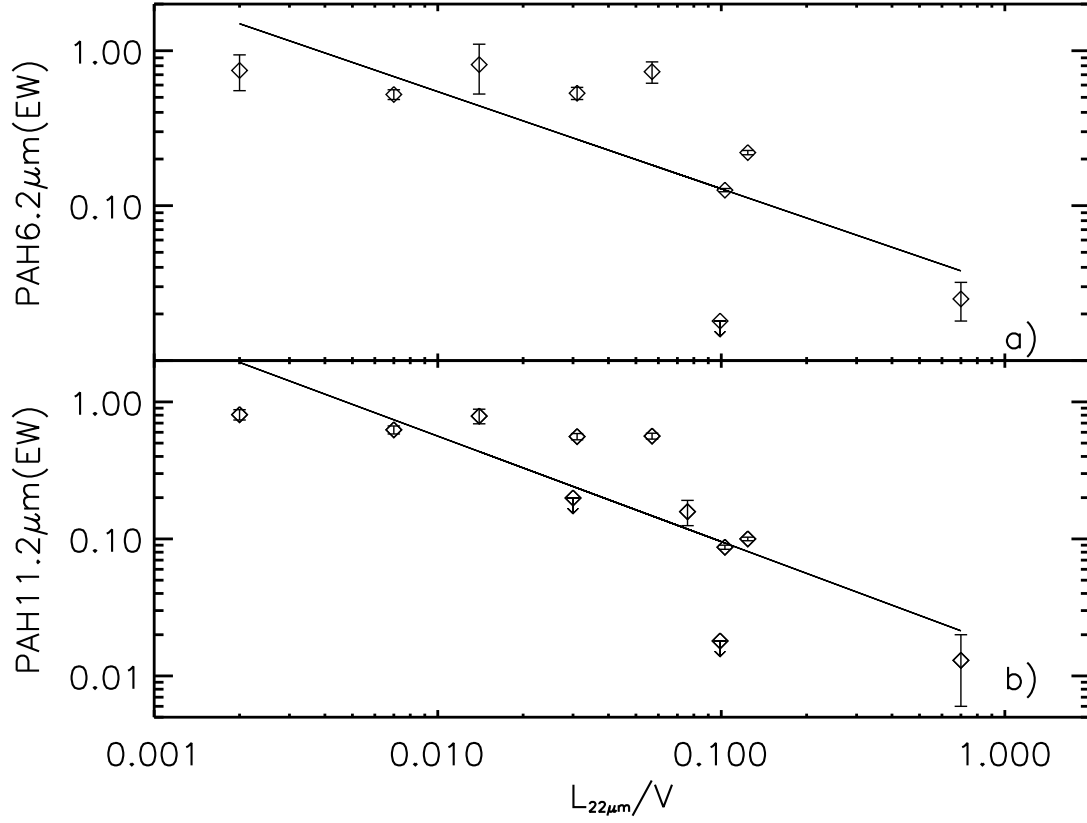
Fig. 12.— a) The EW of the $6.2\,\mu$m PAH vs the luminosity density indicated by $L_{22\mu m}/V$. We can see that there is a general trend that as the luminosity density of the galaxy increases, the PAH EW decreases. b) Same as a) but for the $11.2\,\mu$m PAH.
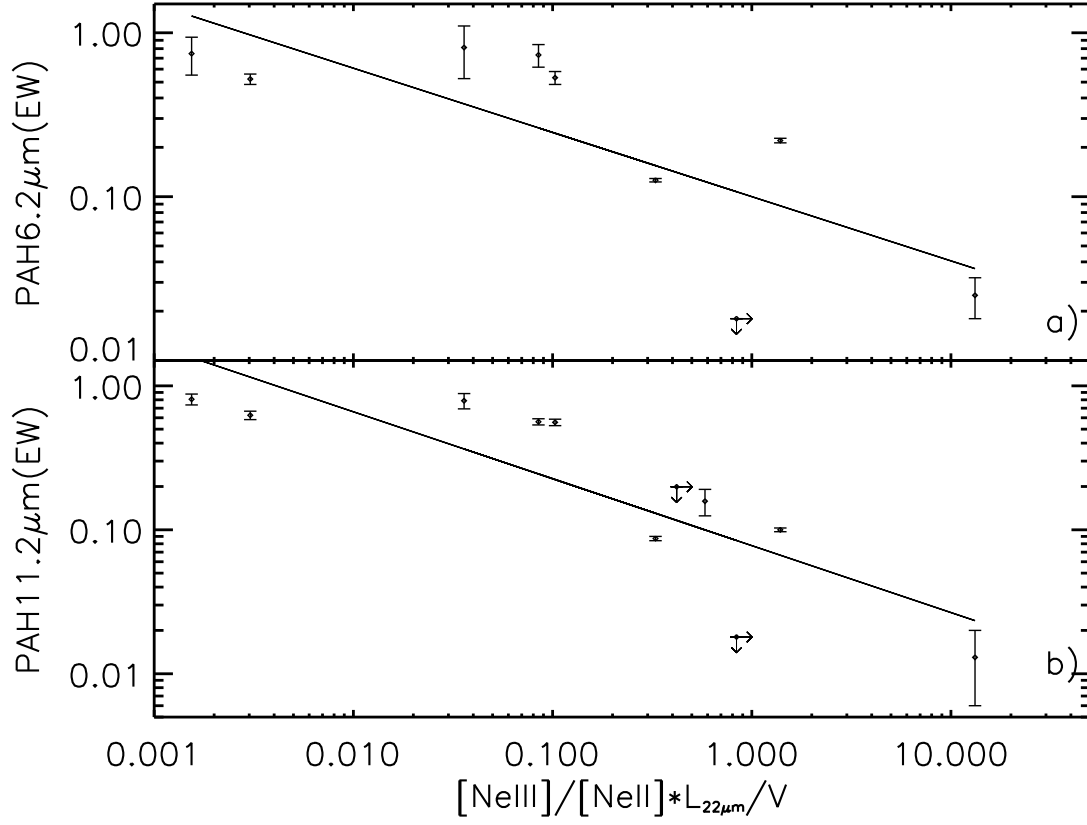
Fig. 13.— a) The dependence of the $6.2\,\mu$m PAH EW on the $([\text{NeIII}]/[\text{NeII}])\times(\text{L}_{22\mu m}/\text{V})$. It is clear that the PAH EW decreases as this quantity increases, indicating that for the same physical volume a more luminous starburst with harder radiation, destroys the PAHs. b) Same as a) but for the $11.2\,\mu$m PAH.

Fig. 14.— a) The PAH EW at $6.2\,\mu$m vs the product of the hardness of the radiation field and the luminosity density, divided by the metallicity of the galaxy. We can see that there is a strong anti-correlation where the PAH EW decreases when the factor ([NeIII]/[NeII])$\times$($L_{22\mu m}$/V)$\times$(1/Z) increases. b) Same as a) but for the $11.2\,\mu$m PAH.

Table 1. Properties of Sources

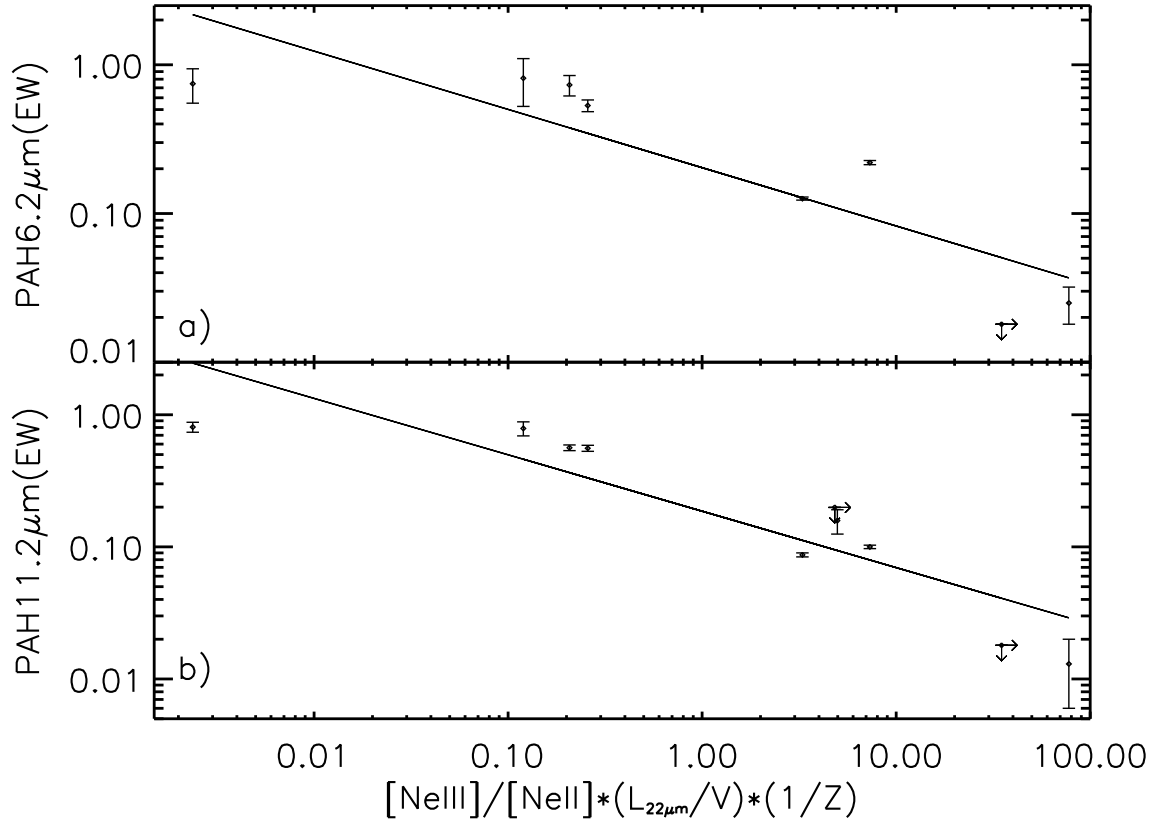| Object Name	RA (J2000)	Dec (J2000)	AORKEY	Observation Date	Redshift	On-source Time (sec)					
						SL	LL	SH	LH	BPU	RPU
Haro11	00h36m52.5s	-33d33m19s	9007104	2004-07-17	0.0206	168	240	480	240	$\cdots$	98
UM283	00h51m49.4s	+00d33m53s	8997888	2004-07-13	0.0155	$\cdots$	$\cdots$	$\cdots$	$\cdots$	28	56
UM133	01h44m41.3s	+04d53m26s	8987392	2004-07-16	0.0054	$\cdots$	$\cdots$	$\cdots$	$\cdots$	28	56
UM382	01h58m09.3s	-00d06m38s	9004032	2005-01-11	0.0118	$\cdots$	$\cdots$	240	120	$\cdots$	$\cdots$
			12628224	2005-01-14		$\cdots$	$\cdots$	$\cdots$	$\cdots$	28	56
			9003776	2004-07-16		$\cdots$	$\cdots$	$\cdots$	$\cdots$	28	56
			8993792	2005-01-11		56	120	$\cdots$	$\cdots$	$\cdots$	$\cdots$
UM408	02h11m23.4s	+02d20m30s	8997120	2004-08-07	0.0120	$\cdots$	$\cdots$	$\cdots$	$\cdots$	28	56
NGC1140	02h54m33.6s	-10d01m40s	4830976	2004-01-07	0.0050	168	240	480	240	$\cdots$	98
SBS0335-052E	03h37m44.0s	-05d02m40s	11769856	2004-09-01	0.0135	$\cdots$	$\cdots$	1440	960	$\cdots$	50
			8986880	2004-02-06		840	420	$\cdots$	$\cdots$	$\cdots$	50
NGC1569	04h30m47.0s	+64d50m59s	9001984	2004-03-01	~ 0	112	120	480	240	$\cdots$	50
IIZw40	05h55m42.6s	+03d23m32s	9007616	2004-03-01	0.0026	168	240	480	240	$\cdots$	98
Tol0618-402	06h20m02.5s	-40d18m09s	4845824	2003-12-15	0.0350	$\cdots$	$\cdots$	$\cdots$	$\cdots$	28	56
SBS0743+591B	07h47m46.7s	+59d00m30s	12625920	2005-03-18	0.0211	$\cdots$	$\cdots$	$\cdots$	$\cdots$	28	56
			12622080	2005-03-20		$\cdots$	$\cdots$	$\cdots$	$\cdots$	28	56
SBS0754+570	07h58m26.4s	+56d54m22s	12630272	2005-03-20	0.0116	$\cdots$	$\cdots$	$\cdots$	$\cdots$	28	56
UGC4274	08h13m13.0s	+45d59m39s	12076032	2004-10-23	0.0015	112	240	120	56	$\cdots$	50
			12626688	2004-11-11		112	240	120	56	$\cdots$	50
SBS0813+582A	08h18m04.5s	+58d05m56s	12629248	2005-03-18	0.0268	$\cdots$	$\cdots$	$\cdots$	$\cdots$	28	56
HS0822+3542	08h25m55.5s	+35d32m32s	12630016	2004-11-11	0.0024	$\cdots$	$\cdots$	$\cdots$	$\cdots$	28	56
IZw18	09h34m02.0s	+55d14m28s	9008640	2004-03-27	0.0025	168	240	480	240	$\cdots$	98
			12622848	2005-04-23		960	480	$\cdots$	$\cdots$	$\cdots$	98
SBS0935+495	09h38m24.0s	+49d18m17s	12624640	2004-11-13	0.0314	$\cdots$	$\cdots$	$\cdots$	$\cdots$	28	56
SBS0940+544	09h44m16.7s	+54d11m33s	9010432	2004-03-26	0.0055	$\cdots$	$\cdots$	$\cdots$	$\cdots$	28	56
SBS0943+563	09h47m13.0s	+56d06m07s	12627200	2004-11-13	0.0253	$\cdots$	$\cdots$	$\cdots$	$\cdots$	28	56
SBS1001+555	10h04m41.8s	+55d18m43s	12624384	2005-04-15	0.0037	$\cdots$	$\cdots$	$\cdots$	$\cdots$	28	56
KUG1013+381	10h16m24.5s	+37d54m46s	4846336	2003-12-15	0.0040	$\cdots$	$\cdots$	$\cdots$	$\cdots$	28	56
			8999168	2004-04-16		$\cdots$	$\cdots$	120	120	$\cdots$	$\cdots$
			9012224	2004-04-16		56	240	$\cdots$	$\cdots$	$\cdots$	$\cdots$
			12628992	2005-04-22		960	$\cdots$	$\cdots$	$\cdots$	50	$\cdots$
SBS1116+597	11h18m47.4s	+59d26m02s	12622592	2004-11-17	$\cdots$	$\cdots$	$\cdots$	$\cdots$	$\cdots$	28	56
[RC2]A1116+51	11h19m34.3s	+51d30m12s	4846592	2003-12-15	0.0044	$\cdots$	$\cdots$	$\cdots$	$\cdots$	28	56
SBS1119+586	11h22m37.8s	+58d19m43s	12631040	2005-04-15	0.0053	$\cdots$	$\cdots$	$\cdots$	$\cdots$	28	56
VIIZw403	11h27m59.9s	+78d59m39s	9005824	2004-12-09	~ 0	168	240	480	240	$\cdots$	50
SBS1129+576	11h32m02.5s	+57d22m46s	12632320	2005-01-06	0.0052	$\cdots$	$\cdots$	$\cdots$	$\cdots$	28	56
SBS1135+598	11h37m43.7s	+59d35m34s	12624896	2004-11-17	0.0327	$\cdots$	$\cdots$	$\cdots$	$\cdots$	28	56
Mrk1450	11h38m35.6s	+57d52m27s	9011712	2004-12-12	0.0032	168	240	480	240	$\cdots$	50
SBS1136+607	11h39m11.5s	+60d30m45s	12622336	2004-11-14	0.0116	$\cdots$	$\cdots$	$\cdots$	$\cdots$	28	56
SBS1137+589	11h40m32.0s	+58d38m32s	12630528	2004-11-17	0.0068	$\cdots$	$\cdots$	$\cdots$	$\cdots$	28	56
SBS1141+576	11h44m16.6s	+57d24m32s	12627456	2005-04-15	0.0310	$\cdots$	$\cdots$	$\cdots$	$\cdots$	28	56
UM461	11h51m33.3s	-02d22m22s	9006336	2005-01-03	0.0035	168	240	480	240	$\cdots$	50
SBS1149+596	11h52m34.0s	+59d22m56s	12623360	2004-11-17	0.0112	$\cdots$	$\cdots$	$\cdots$	$\cdots$	28	56
SBS1150+599	11h53m28.9s	+59d39m57s	12621824	2004-11-17	0.0371	$\cdots$	$\cdots$	$\cdots$	$\cdots$	28	56

Table 1—Continued

Object Name	RA (J2000)	Dec (J2000)	AORKEY	Observation Date	Redshift	SL	LL	SH	LH	BPU	RPU
SBS1159+545	12h02m02.4s	+54d15m50s	4847104	2003-12-15	0.0118	⋯	⋯	⋯	⋯	28	56
			9010176	2004-04-17		⋯	⋯	120	120	⋯	⋯
			9008896	2004-04-17		56	240	⋯	⋯	⋯	⋯
			12629504	2005-04-23		960	⋯	⋯	⋯	50	⋯
SBS1200+589B	12h03m22.6s	+58d41m36s	4824064	2004-01-06	0.0321	⋯	240	⋯	⋯	⋯	98
SBS1210+537A	12h12m55.9s	+53d27m38s	8989952	2004-06-06	⋯	168	240	480	240	⋯	⋯
SBS1211+564	12h13m35.9s	+56d08m35s	12623104	2005-04-21	0.0107	⋯	⋯	⋯	⋯	28	56
SBS1212+563	12h14m48.5s	+56d05m19s	12633088	2005-04-21	⋯	⋯	⋯	⋯	⋯	28	56
Tol1214-277	12h17m17.1s	-28d02m33s	9008128	2004-06-28	0.0260	168	240	480	240	⋯	98
SBS1219+559	12h21m29.0s	+55d38m23s	12631296	2005-04-21	0.0308	⋯	⋯	⋯	⋯	28	56
SBS1221+545B	12h24m23.0s	+54d14m48s	12625152	2005-04-21	0.0187	⋯	⋯	⋯	⋯	28	56
HS1222+3741	12h24m36.7s	+37d24m36s	12630784	2005-01-03	0.0409	⋯	⋯	⋯	⋯	28	56
Tol65	12h25m46.9s	-36d14m01s	4829696	2004-01-07	0.0090	168	240	480	240	⋯	98
SBS1227+563	12h30m07.3s	+56d05m13s	12632832	2005-04-21	0.0153	⋯	⋯	⋯	⋯	28	56
[RC2]A1228+12	12h30m48.5s	+12d02m42s	8998656	2004-06-27	0.0042	⋯	⋯	⋯	⋯	28	56
SBS1235+559	12h37m36.9s	+55d41m04s	12628480	2005-04-21	0.0293	⋯	⋯	⋯	⋯	28	56
UGCA292	12h38m40.0s	+32d46m01s	4831232	2004-01-07	0.0010	168	240	480	240	⋯	98
			12076288	2005-01-03		⋯	⋯	⋯	⋯	28	56
Tol1304-353	13h07m37.5s	-35d38m19s	9006848	2004-06-25	0.0140	168	240	480	240	⋯	50
			12075520	2005-02-10		⋯	⋯	⋯	⋯	28	56
HS1319+3224	13h21m19.9s	+32d08m23s	12625664	2005-02-07	0.0182	⋯	⋯	⋯	⋯	28	56
Pox186	13h25m48.6s	-11d37m38s	9007360	2004-07-14	0.0039	168	240	480	240	⋯	50
			12625408	2005-02-15		⋯	⋯	⋯	⋯	28	56
SBS1415+437	14h17m01.4s	+43d30m05s	4844288	2004-01-07	0.0020	⋯	⋯	⋯	⋯	28	56
			8990464	2004-05-15		⋯	⋯	120	120	⋯	⋯
			9008384	2004-05-13		56	240	⋯	⋯	⋯	⋯
HS1424+3836	14h26m28.1s	+38d22m59s	12628736	2005-02-13	0.0226	⋯	⋯	⋯	⋯	28	56
Mrk475	14h39m05.4s	+36d48m22s	8995840	2004-02-07	0.0019	⋯	⋯	⋯	⋯	28	56
			8996864	2004-06-05		⋯	⋯	120	120	⋯	⋯
			8988672	2004-06-26		56	240	⋯	⋯	⋯	⋯
CG0598	14h59m20.6s	+42d16m10s	8992256	2005-03-19	0.0575	168	240	480	240	⋯	50
CG0752	15h31m21.3s	+47d01m24s	8991744	2005-03-19	0.0211	168	240	480	240	⋯	50
SBS1533+574B	15h34m14.1s	+57d17m04s	12627968	2005-01-09	0.0110	⋯	⋯	⋯	⋯	28	56
SBS1538+584	15h39m56.9s	+58d15m33s	12623616	2005-01-08	0.0435	⋯	⋯	⋯	⋯	28	56
SBS1541+590	15h42m55.8s	+58d55m09s	12631552	2004-12-12	0.0450	⋯	⋯	⋯	⋯	28	56
Mrk1499	16h35m21.1s	+52d12m53s	9011456	2004-06-05	0.0090	168	240	480	240	⋯	98
[RC2]A2228-00	22h30m33.9s	-00d07m35s	9006080	2004-06-24	0.0052	168	240	480	240	⋯	50

[a]The coordinates and redshifts of the objects are cited from The NASA/IPAC Extragalactic Database (NED)(NED is operated by the Jet Propulsion Laboratory, California Institute of Technology, under contract with the National Aeronautics and Space Administration).

Table 2.   Integrated photometry of Sources

Object Name	$f_{8\mu m}$ (mJy)	$f_{16\mu m}$ (mJy)	$f_{22\mu m}$ (mJy)	$f_{24\mu m}$ (mJy)	B (mag)	K (mag)	$f_{22\mu m}/f_{16\mu m}$	$Z/Z_\odot$	References B/K	Z
Haro11	190.0	$\cdots$	851.2[a]	1900	14.31	12.0	$\cdots$	0.1	1) , 2)	19)
UM283	$\cdots$	3.0	8.2	$\cdots$	17.38	$\cdots$	2.7	0.048	9)	24)
UM133	$\cdots$	2.0	6.6	$\cdots$	15.41	$\cdots$	3.4	0.052	3)	25)
UM382	$\cdots$	0.7	1.5	$\cdots$	18.20	$\cdots$	2.2	0.035	3)	25)
UM408	$\cdots$	1.3	3.5	$\cdots$	17.46	$\cdots$	2.7	0.052	3)	25)
NGC1140	$\cdots$	$\cdots$	294.4	$\cdots$	12.56	10.51	$\cdots$	0.4	4) , 5)	14)
SBS0335-052E	11.2	$\cdots$	78.0	66	17.07	$\cdots$	$\cdots$	0.024	10	17)
NGC1569	$\cdots$	$\cdots$	2067.5[a]	$\cdots$	9.42	7.86	$\cdots$	0.19	4) , 6)	16)
IIZw40	105.0	$\cdots$	796.1[a]	1500	11.87	12.35	$\cdots$	0.17	3) , 5)	15)
SBS0743+591B	$\cdots$	2.3	4.7	$\cdots$	$\cdots$	$\cdots$	2.1	$\cdots$		
SBS0754+570	$\cdots$	0.8	2.4	$\cdots$	$\cdots$	$\cdots$	2.9	$\cdots$		
UGC4274	$\cdots$	$\cdots$	130.2	$\cdots$	12.07	9.13	$\cdots$	0.41	4) , 6)	18)[g]
HS0822+3542	0.2	1.3	4.1	2.7	17.92	$\cdots$	3.1	0.028	26)	26)
IZw18	0.7	$\cdots$	4.1	5.5	16.05	15.92	$\cdots$	0.018	3) , 11)	27)
SBS0935+495	$\cdots$	1.2	2.9	$\cdots$	$\cdots$	$\cdots$	2.3	$\cdots$		
SBS0940+544	$\cdots$	1.1	2.3	$\cdots$	17.18	$\cdots$	2.1	0.033	3)	21)
SBS0943+563	$\cdots$	1.4	3.8	$\cdots$	$\cdots$	$\cdots$	2.8	$\cdots$		
KUG1013+381	$\cdots$	6.4	17.1	$\cdots$	16.04	$\cdots$	2.7	0.047	28)	28)
SBS1116+597	$\cdots$	1.0	1.1	$\cdots$	$\cdots$	13.28	1.2	$\cdots$	5)	
[RC2]A1116+51	$\cdots$	0.5	1.7	$\cdots$	17.46	$\cdots$	3.6	0.049	12)	29)
SBS1119+586	$\cdots$	0.6	1.5	$\cdots$	$\cdots$	$\cdots$	2.6	$\cdots$		
VIIZw403	2.5	$\cdots$	7.7	28	14.11	12.7	$\cdots$	0.060	3) , 7)	21)
SBS1129+576	$\cdots$	0.3	1.4	$\cdots$	$\cdots$	$\cdots$	4.0	0.032		30)
SBS1135+598	$\cdots$	0.2	0.8	$\cdots$	$\cdots$	$\cdots$	3.7	$\cdots$		
Mrk1450	2.4	$\cdots$	52.1	48	15.75	$\cdots$	$\cdots$	0.117	3)	21)
SBS1136+607	$\cdots$	0.5	1.8	$\cdots$	$\cdots$	$\cdots$	3.8	$\cdots$		
SBS1137+589	$\cdots$	0.5	1.0	$\cdots$	$\cdots$	$\cdots$	2.2	$\cdots$		
SBS1141+576	$\cdots$	1.1	2.9	$\cdots$	$\cdots$	$\cdots$	2.5	$\cdots$		
UM461	1.6	$\cdots$	29.2	30	$\cdots$	$\cdots$	$\cdots$	0.087		22)
SBS1149+596	$\cdots$	1.5	4.4[b]	$\cdots$	$\cdots$	$\cdots$	3.1	$\cdots$		
SBS1150+599	$\cdots$	0.3	0.6	$\cdots$	$\cdots$	12.67	1.8	$\cdots$	5)	
SBS1159+545	$\cdots$	2.6	6.4	$\cdots$	$\cdots$	$\cdots$	2.5	0.038		21)
SBS1212+563	$\cdots$	1.0	1.2	$\cdots$	$\cdots$	$\cdots$	1.2	$\cdots$		
Tol1214-277	0.2	$\cdots$	3.5	5.5	$\cdots$	$\cdots$	$\cdots$	0.045		24)
SBS1219+559	$\cdots$	1.0	2.1	$\cdots$	$\cdots$	$\cdots$	2.1	$\cdots$		
SBS1221+545	$\cdots$	0.6	1.9	$\cdots$	$\cdots$	$\cdots$	3.0	$\cdots$		
HS1222+3741	$\cdots$	3.0	6.9	$\cdots$	18.40	$\cdots$	2.3	0.054	13)	32)
Tol65	0.9	$\cdots$	15.7	15	17.26	$\cdots$	$\cdots$	0.031	3)	24)
SBS1227+563	$\cdots$	1.0	1.7	$\cdots$	$\cdots$	$\cdots$	1.7	$\cdots$		
[RC2]A1228+12	$\cdots$	1.2	3.4	$\cdots$	17.96	$\cdots$	2.9	0.054	8)	29)
SBS1235+559	$\cdots$	0.3	1.0	$\cdots$	$\cdots$	$\cdots$	2.9	$\cdots$		
Tol1304-353	$\cdots$	6.0	10.8	$\cdots$	$\cdots$	$\cdots$	1.8	0.058		33)
HS1319+3224-	$\cdots$	1.3	2.1	$\cdots$	19.0	$\cdots$	1.6	0.048	13)	32)
Pox186	$\cdots$	5.8	13.1	$\cdots$	17.0	$\cdots$	2.3	0.066	14)	31)

Table 2—Continued

Object Name	$f_{8\mu m}$ (mJy)	$f_{16\mu m}$ (mJy)	$f_{22\mu m}$ (mJy)	$f_{24\mu m}$ (mJy)	B (mag)	K (mag)	$f_{22\mu m}/f_{16\mu m}$	$Z/Z_\odot$	References B/K	Z
SBS1415+437	$\cdots$	6.0	19.6	$\cdots$	15.43	$\cdots$	3.2	0.048	3)	21)
HS1424+3836-	$\cdots$	0.5	1.5	$\cdots$	18.68	$\cdots$	2.8	0.115	13)	32)
Mrk475	$\cdots$	3.2	10.8	$\cdots$	16.20	$\cdots$	3.3	0.105	3)	21)
CG0598	$\cdots$	$\cdots$	23.0	$\cdots$	$\cdots$	13.17	$\cdots$	0.65	5)	23)
CG0752	$\cdots$	$\cdots$	138.9	$\cdots$	$\cdots$	11.73	$\cdots$	$\cdots$	5)	
SBS1533+574B	$\cdots$	21.2	53.4	$\cdots$	16.02	$\cdots$	2.5	0.158	3)	21)
SBS1538+584	$\cdots$	1.4	3.9	$\cdots$	$\cdots$	$\cdots$	2.8	$\cdots$		
SBS1541+590	$\cdots$	1.3	3.3	$\cdots$	$\cdots$	$\cdots$	2.5	$\cdots$		
Mrk1499	$\cdots$	$\cdots$	29.5	$\cdots$	16.00	$\cdots$	$\cdots$	0.3	4)	20) [g]

[a]The 22μm peak-up is saturated.

[b]The error in this value is higher $\sim$10% in the blue and $\sim$15% in the red due to the presence of a bright star.

[c] $\cdots$ indicates that no data are available.

[d]The *IRAC* $8\,\mu$m and *MIPS* $24\,\mu$m flux densities are quoted from Engelbracht et al. (2005).

[e]References for B and K magnitude: 1) Lauberts & Valentijn (1989), 2) Spinoglio et al. (1995), 3) Gil de Paz et al. (2003), 4) De Vaucouleurs et al. (1991), 5) 2Mass Extended Objects. Final Release (2003), 6)Jarrett et al. (2003), 7) Tully et al. (1981), 8) Young & Currie (1998), 9) Vitores et al. (1996), 10) Papaderos et al. (1998), 11) Thuan (1983), 12) Arp & Oconnell (1975), 13) Vennik et al. (2000), 26) Kniazev et al. (2000), 28) Kniazev et al. (1998)

[f]References for metallicity: The metallicity we list here is converted from the oxygen abundance using 12+log[O/H]=8.91 for solar metallicity (Kunth & Östlin 2000). 14) Calzetti (1997), 15) Cerviño & Mas-Hesse (1994), 16) Kobulnicky & Skillman (1997), 17) Izotov et al. (1997b), 18) Ho et al. (1997), 19) Bergvall et al. (2000), 20) Petrosian et al. (2002), 21) Izotov & Thuan (1999), 22) Kniazev et al. (2004), 23) Peimbert & Torres-Peimbert (1992), 24) Gallego et al. (1997), 25) Masegosa et al. (1994), 26) Kniazev et al. (2000), 27) Skillman & Kennicutt (1993), 28) Kniazev et al. (1998), 29) Kinman & Davidson (1981), 30) Guseva et al. (2003), 31) Guseva et al. (2003), 32) Popescu & Hopp (2000), 33) Stasinska & Leitherer (1996)

[g]The oxygen abundance is calculated from [NII]/Hα measurement using the method proposed by Denicoló et al. (2002)

Table 3.   Synthetic flux density of the sources

Object Name	IRAC 8 μm (mJy)	IRS 16 μm (BPU) (mJy)	IRS 22 μm (RPU) (mJy)	MIPS 24 μm (mJy)
IZw18	$\cdots$	2.6±0.1	5.9±0.3	6.5±0.1
SBS0335-052	12.3±0.2	58.1±0.3	79.8±0.3	81.5±0.2
UM461	1.8±0.1	16.9±0.3	34.5±0.2	37.7±0.2
Haro11	164.2±0.1	932.6±0.3	2307.0±4.5	2640.4±6.5
Mrk1450	2.4±0.2	22.0±0.1	53.5±0.2	59.7±0.1
IIZw40	90.1±0.6	763.7±2.4	1481.9±6.9	1624.0±11.5
NGC1569	72.2±0.2	921.8±0.6	2596.0±1.0	2991.0±4.6
Mrk1499	4.2±0.1	12.4±0.1	30.4±0.1	33.8±0.1
NGC1140	28.7±0.3	103.5±0.1	279.5±0.3	316.6±0.2
UGC4274	17.0±0.2	53.1±0.2	120.5±0.7	132.5±0.5
CG0598	7.2±0.1	11.2±0.1	24.8±0.1	28.3±0.1
CG0752	32.9±0.6	63.6±0.2	148.6±0.1	169.9±0.1

Table 4.   Spectroscopic Data of the Sources

Object Name	PAH EW (μm)				Flux[a] ($\times 10^{-16}$W m^{-2})			
	6.2 μm	7.7 μm	8.6 μm	11.2 μm	[SIV](10.51 μm)	[NeII](12.81 μm)	[NeIII](15.55 μm)	[SIII](18.71 μm)
IZw18	$\cdots$	$\cdots$	$\cdots$	$\cdots$	0.06±0.01	<0.011	0.05±0.01	0.021±0.001
SBS0335-052	<0.018	$\cdots$	$\cdots$	<0.018	0.16±0.01	<0.016	0.135±0.004	0.045±0.004
UM461	$\cdots$	$\cdots$	$\cdots$	<0.199	0.47±0.03	<0.021	0.29±0.01	0.09±0.01
Haro11	0.126±0.003	0.241±0.006	0.055±0.003	0.087±0.003	4.6±0.1	3.2±0.1	10.1±0.1	4.81±0.02
Mrk1450	$\cdots$	$\cdots$	$\cdots$	0.158±0.033	0.75±0.02	0.13±0.01	0.96±0.02	0.46±0.01
IIZw40	0.025±0.007	0.069±0.005	0.009±0.003	0.013±0.007	18.6±0.4	0.60±0.03	11.4±0.3	4.7±0.2
NGC1569	0.220±0.007	0.402±0.012	0.045±0.004	0.100±0.003	14.8±0.4	1.55±0.08	17.4±0.3	7.2±0.2
Mrk1499	0.831±0.288	0.997±0.189	0.345±0.049	0.788±0.096	0.18±0.01	0.19±0.01	0.50±0.02	0.30±0.01
NGC1140	0.532±0.048	0.579±0.025	0.142±0.008	0.558±0.029	1.30±0.04	1.17±0.02	3.8±0.1	2.17±0.04
UGC4274	0.732±0.115	0.671±0.040	0.191±0.010	0.563±0.028	0.46±0.02	0.88±0.03	1.31±0.04	1.30±0.03
CG0598	0.746±0.194	0.954±0.075	0.331±0.036	0.807±0.070	0.13±0.02	0.206±0.004	0.18±0.03	0.23±0.01
CG0752	0.522±0.038	0.645±0.024	0.171±0.008	0.625±0.042	0.15±0.01	1.23±0.03	0.58±0.01	0.82±0.02

[a]The integrated fluxes are measured from the high resolution spectra of the targets. Background emission hasn't been subtracted and no scaling between the two modules, SH and LH has been applied.

[b] $\cdots$ indicates no available PAH EW measurement. It is mostly due to the low SNR of the spectrum. In this case, the determination of the continuum is highly uncertain and will significantly change the PAH EW. A much deeper observation with more exposure time has been submitted and more analysis will follow when data come in. For SBS0335-052, the SNR is high enough, but no PAH features can be identified in its mid-IR spectrum. We do not have a template to derive the upper limit of PAH EW at 7.7 μm and 8.6 μm.

Table 5.   Galaxy luminosity and volume

Object	$f_{22\mu m}$[a] (Jy)	Radius[b] (arcsec)	$L_{22\mu m}$[c] ($\times 10^8 L_\odot$)	Volume ($\times 10^9 pc^3$)	$L_{22\mu m}$/Volume ($L_\odot/pc^3$)
IZw18	0.006	7.2	0.01	0.2	0.007
SBS0335-052	0.080	3.8	3.8	3.9	0.099
UM461	0.030	6.8	0.1	0.4	0.030
Haro11	2.307	9.9	249.7	241.4	0.103
Mrk1450	0.053	5.9	0.1	0.2	0.076
IIZw40	1.482	9.5	2.1	0.3	0.700
NGC1569	2.596	55.4	0.2	0.1	0.124
Mrk1499	0.030	6.1	0.6	4.6	0.014
NGC1140	0.279	28.0	1.8	5.8	0.031
UGC4274	0.120	30.5	0.1	0.1	0.057
CG0598	0.025	5.9	20.8	1185.6	0.002
CG0752	0.149	9.9	16.9	258.3	0.007

[a]The 22 μm flux density are calculated using the "synthetic" method.

[b]The radius of the galaxy is measured using the optical image retrieved from the digital sky server(DSS) for point sources. For the four extended sources mentioned earlier, we used their mid-IR size measured from the 22 μm images.

[c]The 22 μm luminosity in the red peak-up filter(18.5-26.0 μm).